Submitted to the Annals of Applied Statistics
arXiv: math.PR/0000000

RICE-DISTRIBUTED AUTOREGRESSIVE TIME SERIES MODELING OF MAGNITUDE FUNCTIONAL MRI DATA

BY DANIEL W. ADRIAN[‡] AND RANJAN MAITRA[*,§] AND DANIEL B. ROWE[†,¶]

Grand Valley State University[‡] and Iowa State University[§] and Marquette University[¶]

Functional magnetic resonance imaging (fMRI) data generally consist of time series image volumes of the magnitude of complex-valued observations at each voxel. However, incorporating Gaussian-based time series models and the Rice distribution – a more accurate model for the data – in the time series have been separated by a distributional "mismatch". We bridge this gap by including pth-order autoregressive (AR) errors into the Gaussian model for the latent real and imaginary components underlying the Rice-distributed magnitude data. Parameter estimation is then done by augmenting the observed magnitude data with the missing phase data in an Expectation-Maximization (EM) algorithm framework, and followed by AR order determination and computation of test statistics for activation detection. Using simulated and experimental low-SNR fMRI data, we compare the performance of this Ricean time series model with a Gaussian AR(p) model for the magnitude data, and also with a complex Gaussian time series model for the entire complex-valued data. Our results show improved parameter estimation and activation detection under the Ricean AR(p) model for the magnitude data than its Gaussian counterpart. The model using the complex-valued data (which is rarely collected in practice) detects activation better than both magnitude-only models but only because it has more data. Thus, while our results here provide for the improved analysis of commonly-collected and archived magnitude-only fMRI datasets, they also argue strongly against the currently routine practice of discarding the phase of the complex-valued fMRI time series, advocating instead for their inclusion in the analysis.

1. Introduction. Functional magnetic resonance imaging (fMRI) is a prominent non-invasive modality for studying human brain function. It is built upon the principle of the Blood Oxygen Level Dependent (BOLD) contrast (Bandettini *et al.*, 1993; Belliveau *et al.*, 1991; Kwong *et al.*, 1992; Ogawa *et al.*, 1990), where firing neurons lead to changes in the blood oxygen levels of neighboring vessels, and the magnetic resonance (MR) signal fluctuates due to the differing magnetic

[*]Research supported in part by the the National Science Foundation CAREER Grant # DMS-0437555 and the National Institutes of Health (NIH) awards #R21EB016212 and #R21EB034184.

[†]Research supported in part by the National Institutes of Health (NIH) award #R21NS087450.

AMS 2000 subject classifications: Primary 60K35, 60K35; secondary 60K35

Keywords and phrases: bilateral finger-tapping motor experiment, EM algorithm, empirical information matrix, hemodynamic response function, Monte Carlo integration, Rice distribution, signal-to-noise ratio

susceptibilities of oxygenated and deoxygenated hemoglobin (Lazar, 2008). Scientists can gain insight on the functional structures of the brain by analyzing time courses of MR signals acquired while a subject performs a designed series of tasks.

The voxel-wise MR signal at each time point is originally complex-valued, containing real and imaginary (or equivalently, magnitude and phase) components. This complex-valued attribute is a consequence of how the data are acquired: the originally measured, complex-valued k-space data (Brown, Kincaid and Ugurbil, 1982; Ljunggren, 1983; Tweig, 1983) consist of the different frequency contributions to the signal from each voxel resulting from magnetic field gradients (Jezzard and Clare, 2001). Then, the application of the inverse Fourier transform (Jain, 1989), a complex-valued operation on the k-space data, separates these frequencies and localizes each voxel's measurements. However, despite the fact that the original signal is complex-valued, statistical analysis of fMRI data is almost always necessarily only on the magnitude data, because the concomitant phase measurements are discarded and irretrievable once the (magnitude) data are extracted from the scanner (where it is overwritten by subsequent scans). We refer to such analyses as "magnitude-only" (MO) statistical analyses, and note that this approach likely arises as a consequence of the default output of MR scanners that does not routinely include phase images, even though they can easily be collected by simply changing a preset variable in an input file (Yu *et al.*, 2018). Consequently, most fMRI data and analyses are MO, and, at least figuratively, do not use half of the originally available data.

One of the most common forms of MO analysis fits, at each voxel, a general linear model (Friston *et al.*, 1995) for the (preprocessed) time series observations in terms of a waveform representing the expected BOLD contrast. This waveform is the convolution of the stimulus time course with the hemodynamic response function (HRF), which gives the BOLD response to an instantaneous neuronal activation (Friston, Jezzard and Turner, 1994; Glover, 1999). These general linear models for magnitude fMRI time series also incorporate autoregressive (AR) (Bullmore *et al.*, 1996; den Dekker *et al.*, 2009; Marchini and Ripley, 2000) or autoregressive moving average (ARMA) (Locascio *et al.*, 1997) errors, due to several reasons. For one, the hemodynamic response to a single neural activation takes between 15 and 20 seconds (Lazar, 2008), which is much longer than the sampling intervals of many fMRI techniques — for instance, of between 100 milliseconds and five seconds for echo-planar imaging (EPI) techniques (Friston, Jezzard and Turner, 1994). Additional sources of autocorrelation are also provided by the subject's cardiac and respiratory cycles (Friston *et al.*, 2000), and by the common pre-processing step of temporal smoothing. From these model fits, the time series at each voxel is aggregated to a test statistic that measures the degree of activation in the Statistical Parametric Mapping (SPM) framework of Friston *et al.* (1990). Thresholding

methods are then applied to the SPM to identify activated voxels (Genovese, Lazar and Nichols, 2002; Logan and Rowe, 2004; Worsley *et al.*, 1996).

The above MO approaches assume that the magnitude measurements follow a Gaussian distribution, but a more correct model utilizes the Rice distribution (Gudbjartsson and Patz, 1995; Rice, 1944), as we show in the following. It is well-known (Henkelman, 1985; Macovski, 1996; Sijbers *et al.*, 1998) that the complex k-space data are Gaussian distributed, and this distributional assumption is also preserved, by linearity, upon applying an inverse Fourier transform. Specifically, it is commonly assumed (Wang and Lei, 1994) that the real and imaginary measurements at a single point in space and time are independent normal random variables with the same variance and phase-coupled means; it follows that the magnitude has a Rice distribution. The Gaussian MO model is often justified by the fact that the Rice distribution approaches the Gaussian distribution for large signal-to-noise ratios (SNRs).

However, fMRI scans that are more detailed, acquired faster or on portable systems (Liu *et al.*, 2021), come at the loss of SNR. For magnitude fMRI time series, the SNR represents the ratio of the mean, that is, the non-activation-related, baseline signal to the standard deviation (SD) of the noise time series.[1, 2] It is well-known that SNR is proportional to voxel volume and inversely proportional to image acquisition time (Lazar, 2008). Thus, although scans with increased spatio-temporal resolution show promise in a clinical setting in pre-surgical mapping and also in understanding human neuropsychology (Rosen and Savoy, 2012), they also come at the cost of decreased SNR. SNR is also proportional to magnetic field strength, so ultra-high-field (UHF) MRI (Balchandani and Naidich, 2015) makes high-resolution fMRI more feasible, but UHF scanners presently lack wide availability (Cosottini and Roccatagliata, 2021). There has also lately been the move to make MRI (and fMRI) more accessible through the use of ultra-low field magnets (Liu *et al.*, 2021), which while providing more accessible, cost-effective, and environmentally sustainable scanning equipment, however yield images of relatively poor quality, lower SNR and limited spatial resolution (Islam *et al.*, 2023).

Out of the above concern that the Gaussian assumption may not be adequate for such low-SNR data, Zhu *et al.* (2009) developed Rice-distributed models that ignored temporal dependence in the voxel-wise time series, with Bayesian methodology for this problem also developed in Wegmann, Eklund and Villani (2017). Also, Solo and Noh (2007) demonstrated that Gaussian-model-based maximum

[1]There is also the contrast-to-noise ratio, or CNR, that is the ratio of the amplitude of the BOLD contrast to the noise SD.

[2]It should be noted that we are speaking of temporal SNR – comparing measurements across time at a single voxel – and not image SNR, which would compare measurements across voxels at a single time point; see Murphy, Bodurka and Bandettini (2007).

likelihood (ML) estimates of parameters for simulated Ricean data are biased for SNRs under 5, with the bias increasing as the SNR decreases. But, a Ricean model for the observations that also incorporates temporal dependence has never previously been developed, and we address this lacuna in this paper.

1.1. *Main contributions of this paper.* We highlight the main contributions to the statistics and scientific community that we make through this paper. First, we provide methodology and analyze the use of autoregressive time series regression for data that are from the Rice distribution. In doing so, we address the gaps in Zhu *et al.* (2009) or in Wegmann, Eklund and Villani (2017) that ignored temporal structure while developing Rice-based regression models for the fMRI time series. Adrian, Maitra and Rowe (2018) showed substantial gains in using the complex-valued data over those using (Gaussian-distribution-assumed) MO-only data, however, all archived or acquired datasets from fMRI studies are MO, and therefore it is important to see if the analysis of such datasets can be improved by using more accurate Rice-distributed AR time series models, especially in low-SNR situations.

Second, we provide a thorough and detailed comparison of the CV-based analysis (Adrian, Maitra and Rowe, 2018) of fMRI data vis-a-vis that obtained using the methods developed in this paper. We show that while our Rice-distributed modeling of MO datasets improves parameter estimation and activation detection accuracy, over those done by Gaussian-based MO analysis, with the improvement very pronounced at low SNRs, both analyses approaches are outperformed by CV-based analysis. Therefore, we advocate to the fMRI and scientific community for the storage (and analysis) of CV (both magnitude and phase) fMRI data, especially because, as mentioned earlier, its acquision is a simple matter of modifying a preset variable in an input file (Yu *et al.*, 2018). At the same time, it is important to reiterate, as in the previous paragraph, that archived datasets or those gathered under current practice, only have the magnitude values, with the phase having been discarded and therefore unretrievable, and so need the methods developed in this paper for their improved MO-based analysis.

Third, as will be discussed in Section 2, we provide to the community not only a complex-valued fMRI dataset of a finger-tapping experiment, but one that, with the innovative use of a radio-frequency (RF) coil, provides us with a low-SNR dataset of a well-studied experiment, and allows for benchmarking of performance of our more accurate MO-based methods in lower-SNR frameworks. Ultra-low-field MRI is increasingly gaining popularity, however these systems are mostly unavailable publicly, and our framework fills this gap, providing a CV dataset with both magnitude and phase measurements.

Fourth, but also significant, our immediate application in this paper is in the context of analyzing fMRI time series, but similar problems also arise in the context

of signal processing and communications (Abdi *et al.*, 2001; Arafa and Messier, 2010; Bar-Shalom, Li and Kirubarajan, 2001; Hajri, Youssef and Patzold, 2009; Lindsey, 1964) where it may be desirable to understand the characteristics and behavior of wireless, radar and sonar signals in relation to other factors. Another context is in meteorology (Baïle, Muzy and Poggi; Best, Rayner and Thas, 2010; , 2024) where first the Rayleigh and then the Rice and the M-Rice distributions have lately been used to better model the windspeed, and improving regression modeling of Rice-based time series data are important, for instance for predicting windspeed and wind energy energy output (Wang *et al.*, 2019).

1.2. *Organization of this paper.* The remainder of the paper is structured as follows. Section 2 introduces a series of low-SNR images acquired from a finger-tapping experiment that is our motivating application. These images have a lower SNR than typical fMRI data due to their being acquired with the body coil instead of the head coil, and their analysis here is motivated by the divergence of the Rice and Gaussian distributions at low SNRs. Section 3 illustrates the novel methodological development of the MO AR(p) Ricean model. Section 4 performs simulation experiments to study the validity of the methodological results and compares the results using different models, under a known ground truth. We compare three models: the AR(p) Ricean and Gaussian models for MO voxel time series, as well as a model that utilizes the entire complex-valued (CV) data. Our primary focus is on the two models for MO data, as the entire CV data is rarely collected, but we also present comparisons between the CV versus MO data-based models to advocate for collecting the complete data. Section 5 presents the statistical analysis of the low-SNR dataset and its implications. We conclude with a discussion of the results and the paper. Our paper also has a supplement containing additional details regarding methodology, the simulation experiments, and the dataset analysis. Sections, figures, and equations in the supplement are referenced here with the prefix "S-".

2. A low-SNR fMRI finger-tapping experiment dataset.

2.1. *Data acquisition.* We develop our methods in the backdrop of a sequential finger-tapping experiment, the type of which are applied to noninvasive neurosurgical preparation (Lee *et al.*, 1999). Experiments that use finger tapping, sponge squeezing, or brushing of the palms as stimuli in block design are used to identify the location of hand function in candidate patients for resective surgical treatment for tumors and epilepsy (Lee, Jack and Riederer, 1998). While it is well-known that the central sulcus in the sensorimotor cortex is the location of hand function for normal healthy adults (Rumeau *et al.*, 1994), fMRI allows the location of specific

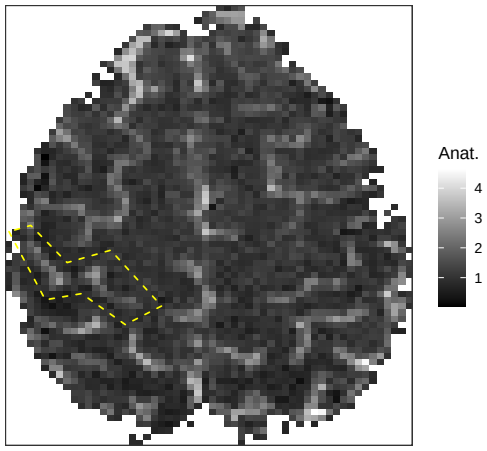

FIG 1. *Anatomical image of the second slice identifying the left central sulcus.*

functional areas to be verified noninvasively in relation to the proposed surgical target (Lee *et al.*, 1999).

In our application, MR images were acquired with TR = 1s during a block design experiment with an initial 16s of rest followed by 19 epochs of 16s of right-hand finger tapping alternating with 16s of rest. Following standard practice, the first three images are excluded from our analysis due to machine "warmup" effects, leaving us with a temporal sequence of $n = 621$ images. Each volume image was composed of seven 2.5 mm thick 128×128 axial slices with a 24.0 cm FOV. Due to the decussation of nerve fibers in the upper slices of the brain, crossing from one lateral side to the other (Carpenter, 1991), the right-hand finger tapping activates the left central sulcus (identified in Figure 1).

The data were acquired with the body coil (also known as the RF coil, as it produces the radiofrequency pulse used to produce the "resonance" condition of MRI). In general, the body coil has a large measurement field, and thus has lower SNR than specialized coils such as the head coil usually used in fMRI studies. Health care sites in developing countries may use body coil acquisition because specialized coils represent additional costs beyond the MR scanner. Additionally, spinal (Powers, Ioachim and Stroman, 2018) and renal fMRI (Zhang *et al.*, 2013) use body coil acquisition. Using body (rather than head) coil acquisition provides us with a lower SNR dataset of a well-studied experiment to serve as a marker for performance in low-SNR settings, which is where CV, MO Ricean and MO Gaussian models have been shown to diverge previously. Further, as mentioned in Section 1.1, it is extremely rare for such a dataset to be publicly available, so we make it available to the scientific community at https://github.com/dadrian14/arp-

rice-data.

2.2. *Data processing pipeline.* For this dataset, the phase components of the time series images were not discarded but stored along with the magnitude images used in traditional fMRI analysis. The data processing flow included Nyquist ghost removal and correction for global zero-order off-resonance using three navigator echos (Jesmanowicz, Wong and Hyde, 1993; Nencka, Hahn and Rowe, 2008), image reconstruction from k-space by inverse Fourier transform (Kumar, Welti and Ernst, 1975; Rowe, 2016), and estimation and correction of the dynamic field using temporal off-resonance alignment of single-echo timeseries (TOAST) (Hahn, Nencka and Rowe, 2009, 2012). A binary mask of voxels above 12% of the maximum voxel signal magnitude was generated from the first magnitude image of the dataset (before discarding the first three images) to represent the voxels within the brain subject to statistical activation detection. In addition, we used smoothing splines to detrend the voxel time series, after comparing several methods (see Section S-1.1).

After preprocessing, we applied the CV and MO models to each voxel time series. For each model, the design matrix $\boldsymbol{X}$ had $n = 621$ rows and $q = 2$ columns: one column was an intercept modeling the baseline MR signal and the other was a zero-centered waveform modeling the expected BOLD repsonse given by a convolution of the stimulus time course with the Glover (1999) hemodynamic response function. The bottom panel of Figure S-1 shows a superposition of the block design stimulus time course with this expected BOLD response waveform. The next section presents these CV and MO time series models in detail.

3. Methodological development. We compare three models for fMRI time series: the AR(p) Ricean and Gaussian models for MO voxel time series, as well as a model that utilizes the entire complex-valued (CV) data. However, the AR(p) Ricean model and its estimation needs development, so we use this section to do so.

3.1. *Statistical models for CV and MO time series.* We first introduce notation, focusing on a single voxel (and suppressing voxel-related subscripts). The CV measurement at time t can be denoted in real/imaginary form by $y_{Rt} + iy_{It}$ or in magnitude/phase form by $r_t \exp(i\phi_t) = r_t(\cos\phi_t + i\sin\phi_t)$. Trigonometric identities in the complex plane hold that $y_{Rt} = r_t \cos\phi_t$, $y_{It} = r_t \sin\phi_t$, $r_t = (y_{Rt}^2 + y_{It}^2)^{\frac{1}{2}}$, and $\phi_t = \arctan_4(y_{It}, y_{Rt})$, the 4-quadrant arctangent (see Glisson, 2011, Page 348) corresponding to $\arctan(y_{It}/y_{Rt})$. We denote the real, imaginary, magnitude, and phase time series vectors by $\boldsymbol{y}_R = (y_{R1}, \ldots, y_{Rn})'$, $\boldsymbol{y}_I = (y_{I1}, \ldots, y_{In})'$, $\boldsymbol{r} = (r_1, \ldots, r_n)'$, and $\boldsymbol{\phi} = (\phi_1, \ldots, \phi_n)'$, with n denoting

the number of MR scans. The Rowe and Logan (2004) model states that

$$\begin{pmatrix} \boldsymbol{y}_R \\ \boldsymbol{y}_I \end{pmatrix} = \begin{pmatrix} \boldsymbol{X} & \boldsymbol{0} \\ \boldsymbol{0} & \boldsymbol{X} \end{pmatrix} \begin{pmatrix} \boldsymbol{\beta}\cos\theta \\ \boldsymbol{\beta}\sin\theta \end{pmatrix} + \begin{pmatrix} \boldsymbol{\eta}_R \\ \boldsymbol{\eta}_I \end{pmatrix}, \tag{1}$$

where the expected magnitude response $\boldsymbol{X\beta}$ is coupled with the constant phase location parameter θ. The columns of $\boldsymbol{X}$ represent various components of the magnitude signal including the baseline level and the expected BOLD contrast. The errors $\boldsymbol{\eta} = (\boldsymbol{\eta}_R', \boldsymbol{\eta}_I')' \sim \mathcal{N}(\boldsymbol{0}, \boldsymbol{\Sigma} \otimes \boldsymbol{\Phi})$, where $\boldsymbol{\Sigma}$ and $\boldsymbol{\Phi}$ are matrices of order 2 and n, specifying the real/imaginary and temporal covariances (the latter with an AR(p) structure), and the direct (Kronecker) product $\otimes$ implies separability of these covariances. Based on this framework, we present three models:[3]

1. **Complex-valued AR(p) (CV) model**: This model takes the form of (1) with an AR(p) structure for $\boldsymbol{\Phi}$ and $\boldsymbol{\Sigma} = \sigma^2 \boldsymbol{I}_2$. We denote the AR coefficients by $\boldsymbol{\alpha} = (\alpha_1, \ldots, \alpha_p)'$.
2. **Magnitude-only AR(p) Ricean (MOR) model**: The MOR model is the MO (marginal) counterpart of the CV model; in other words, under the MOR model, the latent real and imaginary time series follow the CV model. Under the MOR model, the probability density function (PDF) of magnitude measurements r_t is

$$f(r_t; \mu_t, \gamma_0) = \frac{r_t}{\gamma_0} \exp\left[\frac{-(r_t^2 + \mu_t^2)}{2\gamma_0}\right] \mathbb{I}_0\left(\frac{\mu_t r_t}{\gamma_0}\right), \tag{2}$$

   where $\mu_t = \boldsymbol{x}_t'\boldsymbol{\beta}$, $\boldsymbol{x}_t'$ is the tth row of $\boldsymbol{X}$, $\gamma_0 = Var(\eta_{Rt}) = Var(\eta_{It})$ is zeroth order autocovariance of the latent real and imaginary errors, and $\mathbb{I}_0(\cdot)$ is the modified Bessel function of the first kind and the zeroth order.
3. **Magnitude-only AR(p) Gaussian (MOG) model**: This model assumes $\boldsymbol{r} = \boldsymbol{X\beta} + \boldsymbol{\epsilon}$, where $\boldsymbol{\epsilon}$ follows an AR(p) structure.

These three models are summarized in Table 1, which lists the key features that differentiate them. These features are as follows:

1. *Twice the quantities*: The CV model uses the real and imaginary measurements at each voxel and time-point, while the MOR/MOG models use only the magnitudes, so the CV model uses *twice the quantities* of the MO data-based models. (This does not necessarily mean that twice the amount of useful information is present in the CV over the MO data, especially for models of magnitude-related activation.[4])

[3] For brevity, the distinction between the notations of corresponding parameters in different models is dropped.

[4] Rowe (2005a) introduces fMRI models that allow for activation in both the magnitude and phase data.

		Model features	
Model	Model Abbrev.	Twice the Quantities	Ricean magnitudes
Complex-valued AR(p)	CV	✓	✓
Magnitude-only Ricean AR(p)	MOR		✓
Magnitude-only Gaussian AR(p)	MOG		

TABLE 1

Summary of the three models compared in this paper for complex-valued (CV) and magnitude-only (MO) fMRI data and the features present in each model. These features are italicized whenever they appear in the text.

2. *Ricean magnitudes*: The MOR model assumes the magnitude measurements are Ricean distributed, while the MOG model uses a Gaussian approximation. The CV model also has Rice-distributed magnitudes.

Table 1 illustrates the hierarchical pattern of the features present across the three models. As a result, comparing results for the CV/MOR models allows us to isolate the influence of having *twice the quantities* in the CV data. Similarly, comparing the MOR/MOG models shows the result of the Gaussian approximation of the *Ricean magnitudes*.

3.2. *Parameter Estimation.* Of the three models introduced in Section 3.1, we focus on the methodology of the MO Ricean AR(p) (or MOR) model due to its novelty. We relegate methodological discussions of the CV and MOG models to Section S-2.1.

The methodology for the Ricean AR(p) model fits nicely into the framework of the EM algorithm (Dempster, Laird and Rubin, 1977; McLachlan and Krishnan, 2008) with $\boldsymbol{r}$, $\boldsymbol{\phi}$, and $(\boldsymbol{r}, \boldsymbol{\phi})$ playing the roles of the observed, missing, and complete data, respectively. And because the EM algorithm and its extensions serve as our "workhorse" methodology for the Ricean AR(p) model, we review it briefly here. An iteration of the EM algorithm consists of the Expectation (E-) and Maximization (M-) steps. At the $(k+1)$th iteration, the E-step calculates the objective function $Q(\boldsymbol{\tau}; \boldsymbol{\tau}^{(k)}) = \mathbb{E}_{\boldsymbol{\phi}|\boldsymbol{r},\boldsymbol{\tau}^{(k)}}[\log f(\boldsymbol{r}, \boldsymbol{\phi}; \boldsymbol{\tau})]$, the expectation of the complete data log-likelihood with respect to the conditional distribution $\boldsymbol{\phi}|\boldsymbol{r}$ at the current parameter estimates $\boldsymbol{\tau}^{(k)}$. The M-step calculates the updated parameter values $\boldsymbol{\tau}^{(k+1)} = \operatorname{argmax}_{\boldsymbol{\tau}} Q(\boldsymbol{\tau}; \boldsymbol{\tau}^{(k)})$ by maximizing the objective function. We denote the vector of parameters by $\boldsymbol{\tau} = (\boldsymbol{\alpha}', \boldsymbol{\beta}', \sigma^2)'$. The EM algorithm has well-known favorable properties such as monotone increase of the likelihood for each iteration and reliable global convergence (McLachlan and Krishnan, 2008).

3.2.1. *EM algorithm for ML estimation under the MO AR(p) Ricean model.* In this estimation procedure, we assume a known AR order p, after following the methods described in Section 3.4. To compute starting values $\boldsymbol{\tau}^{(0)}$, we use the

MOG model as demonstrated in Section S-2.1.2. With the algorithm initialized, the E- and M-steps are as follows.

E-step. The complete data log-likelihood can be shown to be

$$\log f(\boldsymbol{r}, \boldsymbol{\phi}; \boldsymbol{\tau}) = -n \log \sigma^2 - \log |\boldsymbol{R}_n| - h/2\sigma^2, \tag{3}$$

(Miller, 1995; Pourahmadi, 2001) where $h = \tilde{\boldsymbol{\alpha}}' \boldsymbol{D} \tilde{\boldsymbol{\alpha}}$, with $\tilde{\boldsymbol{\alpha}}$ as the $(p+1)$-vector $(1, -\alpha_1, \ldots, -\alpha_p)$, and $\boldsymbol{D}$ the $(p+1) \times (p+1)$ symmetric matrix with (i,j)th element

$$d_{ij} = \sum_{t=1}^{n-i-j} \begin{bmatrix} r_{t+i} r_{t+j} \cos(\phi_{t+i} - \phi_{t+j}) - \mu_{t+i} r_{t+j} \cos(\phi_{t+j} - \theta) \\ -\mu_{t+j} r_{t+i} \cos(\phi_{t+i} - \theta) + \mu_{t+i} \mu_{t+j} \end{bmatrix}, \tag{4}$$

where $\mu_t = \boldsymbol{x}_t' \boldsymbol{\beta}$, $\boldsymbol{x}_t'$ is the tth row of $\boldsymbol{X}$. In view of (3) and (4), the E-step involves two kinds of expectations: the univariate expectations $\mathbb{E}[\cos(\phi_t - \theta) | r_t; \boldsymbol{\tau}^{(k)}]$, $t = 1, \ldots, n$, and the bivariate expectations $\mathbb{E}[\cos(\phi_t - \phi_{t+j}) | r_t, r_{t+j}; \boldsymbol{\tau}^{(k)}]$, $j = 1, \ldots, p$, $t = 1, \ldots, n-j$. The univariate expectations can be shown (Section S-2.3.1) to be

$$\mathbb{E}_{\phi_t | r_t; \boldsymbol{\tau}^{(k)}}[\cos(\phi_t - \theta)] = \mathbb{A}(\mu_t^{(k)} r_t / \gamma_0^{(k)}), \qquad t = 1, \ldots, n,$$

where $\mathbb{A}(\xi) = \mathbb{I}_1(\xi)/\mathbb{I}_0(\xi)$, with $\mathbb{I}_m(\xi)$ being the mth order modified Bessel function of the first kind (Abramowitz and Stegun, 1965) evaluated at ξ.

The bivariate expectations are more cumbersome to obtain. First, we reduce $\mathbb{E}_{\phi_t, \phi_{t+j} | r_t, r_{t+j}; \boldsymbol{\tau}^{(k)}}[\cos(\phi_t - \phi_{t+j})]$ to the univariate expectation

$$\mathbb{E}_{\phi_t | r_t, \boldsymbol{\tau}^{(k)}} \left\{ \frac{\mathbb{A}(K(\phi_t))}{K(\phi_t)} [\kappa \cos(\phi_t - \theta) + \delta] \right\}, \tag{5}$$

where $K(\phi_t) = [\kappa^2 + \delta^2 + 2\kappa\delta \cos(\phi_t - \theta)]^{1/2}$, $\kappa = r_{t+j}(\gamma_0^{(k)} \mu_{t+j}^{(k)} - \gamma_j^{(k)} \mu_t^{(k)})/b^{(k)}$, and $\delta = \gamma_j^{(k)} r_t r_{t+j} / b^{(k)}$, with $b^{(k)} = \gamma_0^{2(k)} - \gamma_j^{2(k)}$. (See Section S-2.3.2 for more details.) Because (5) cannot be evaluated analytically, we approximate it via the Delta Method (Casella and Berger, 2002): $\mathbb{E}[f(X)] \approx f[\mathbb{E}(X)]$. When applied to (5), the Delta Method substitutes $\mathbb{A}(r_t \mu_t^{(k)} / \gamma_0^{(k)})$ for each instance of $\cos(\phi_t - \theta)$, including those in the $K(\phi_t)$ terms.

M-step. The global maxima of the objective function is not of closed form, so we obtain $\boldsymbol{\tau}^{(k+1)}$ through three conditional maximization steps as in the ECM algorithm (Meng and Rubin, 1993). First, we calculate the updated estimate $\boldsymbol{\alpha}^{(k+1)}$ via the equations

$$\sum_{j=1}^{p} \left(d_{ij}^{(k)} + 2j \gamma_{|j-i|}^{(k)} \right) \alpha_j = d_{i0}^{(k)}, \quad i = 1, \ldots, p, \tag{6}$$

where $d_{ij}^{(k)}$ is the E-step expectation of d_{ij} with μ_t evaluated at $\mu_t^{(k)}$ and $\gamma_j^{(k)} = d_{0j}^{(k)}/(2n)$. Next, we calculate

$$\boldsymbol{\beta}^{(k+1)} = (\boldsymbol{X}'\boldsymbol{R}_n^{-1}\boldsymbol{X})^{-1}\boldsymbol{X}'\boldsymbol{R}_n^{-1}\boldsymbol{u}^{(k)}, \tag{7}$$

where $\boldsymbol{R}_n^{-1}$ is obtained from $\boldsymbol{\alpha}^{(k+1)}$ (as in Pourahmadi, 2001) and $\boldsymbol{u}^{(k)}$ is a vector of n variables with tth element $u_t^{(k)} = r_t\mathbb{A}(r_t\mu_t^{(k)}/\gamma_0^{(k)})$. Note that it may be necessary to enforce the boundary conditions $\boldsymbol{X}\boldsymbol{\beta}^{(k+1)} \geq \boldsymbol{0}$, in which case (7) needs to be modified as discussed in Section S-2.3.3. Finally, we calculate $\sigma^{2(k+1)} = h^{(k+1)}/(2n)$, where $h^{(k+1)} = \tilde{\boldsymbol{\alpha}}'^{(k+1)}\boldsymbol{D}^{(k+1)}\tilde{\boldsymbol{\alpha}}^{(k+1)}$ and $\boldsymbol{D}^{(k+1)}$ is a matrix as before with terms $d_{ij}^{(k+1)}$ evaluated using $\mu_t^{(k+1)} = \boldsymbol{x}_t'\boldsymbol{\beta}^{(k+1)}$.

3.2.2. *Hybrid algorithm for ML estimation.* As the EM algorithm progresses through iterations, we monitor convergence using the maximum change in the parameter values across successive iterations. However, as is commonly known (McLachlan and Krishnan, 2008) the convergence of the EM algorithm is slow at low SNRs, especially when $\beta_0/\sigma < 2$. In order to speed up convergence, we employ the hybrid algorithm of Aitkin and Aitkin (1996) which alternates the EM iterations with those from a modified Newton-Raphson (NR) method where the Fisher information matrix is replaced by the empirical information matrix (Meilijson, 1989). The hybrid algorithm starts with five EM iterations before switching to the modified NR method until convergence of the parameters. In the latter case, we halve the NR step size up to five times.

Parameter updates from the modified Newton-Raphson method are given by

$$\boldsymbol{\tau}^{(k+1)} = \mathscr{I}_e^{-1}(\boldsymbol{\tau}^{(k)};\boldsymbol{r})\boldsymbol{S}(\boldsymbol{r};\boldsymbol{\tau}^{(k)}), \tag{8}$$

where $\mathscr{I}_e(\boldsymbol{\tau};\boldsymbol{r})$ is the empirical information matrix and $\boldsymbol{S}(\boldsymbol{r};\boldsymbol{\tau})$ is the score statistic. Both are constructed from the contributions to the score statistic at $t{=}p{+}1, p{+}2, \ldots, n$, denoted by $\boldsymbol{s}(r_t;\boldsymbol{\tau}) = \frac{\partial}{\partial\boldsymbol{\tau}}\log f(r_t|r_{t-1},\ldots,r_{t-p};\boldsymbol{\tau})$, which can be calculated from the complete data loglikelihood using the identity (adapted from McLachlan and Krishnan, 2008)

$$\boldsymbol{s}(r_t;\boldsymbol{\tau}) = \mathbb{E}_{\boldsymbol{\phi}|\boldsymbol{r};\boldsymbol{\tau}}\left[\frac{\partial}{\partial\boldsymbol{\tau}}\log f((r_t,\phi_t)|(r_{t-1},\phi_{t-1}),\ldots,(r_{t-p},\phi_{t-p});\boldsymbol{\tau})\right]. \tag{9}$$

These calculations, detailed in Section S-2.3.4, use quantities from the E-step. The empirical information matrix is calculated as

$$\mathscr{I}_e(\boldsymbol{\tau};\boldsymbol{r}) = \sum_{t=p+1}^{n}\boldsymbol{s}(r_t;\boldsymbol{\tau})\boldsymbol{s}'(r_t;\boldsymbol{\tau}) - \frac{1}{n-p}\boldsymbol{S}(\boldsymbol{r};\boldsymbol{\tau})\boldsymbol{S}'(\boldsymbol{r};\boldsymbol{\tau}), \tag{10}$$

where $\boldsymbol{S}(\boldsymbol{r};\boldsymbol{\tau}) = \sum_{t=p+1}^{n}\boldsymbol{s}(r_t;\boldsymbol{\tau})$.

3.3. *Calculation of test statistics under the MO AR(p) Ricean model.* We illustrate the calculations of Wald and likelihood ratio test statistics for a general test for activation, which posits $H_0 : \boldsymbol{C\beta} = \mathbf{0}$ against $H_a : \boldsymbol{C\beta} \neq \mathbf{0}$. Each test statistic is based on the MLEs $\widehat{\boldsymbol{\tau}}$ calculated by the above EM/NR hybrid algorithm.

3.3.1. *Wald test.* The Wald test statistic is given by

$$W = (\boldsymbol{C}\widehat{\boldsymbol{\beta}})' \left[\boldsymbol{C}\mathscr{I}_e^{-1}(\widehat{\boldsymbol{\tau}}; \boldsymbol{r})\boldsymbol{C}'\right]^{-1} (\boldsymbol{C}\widehat{\boldsymbol{\beta}}), \tag{11}$$

and asymptotically follows a null χ^2_m-distribution, where m is the rank of $\boldsymbol{C}$. It utilizes the empirical information matrix $\mathscr{I}_e$ of (10). However, our simulation studies reported in Section S-2.4.1 indicate that the Wald test statistic does not follow this null distribution for low-SNR time series, that is, when $\beta_0/\sigma < 2$. This shortcoming of the Wald test motivates the derivation of the likelihood ratio test (LRT) statistic described below.

3.3.2. *Likelihood ratio test for Ricean AR(1) model.* We derive an LRT for the Ricean AR(1) model, whose false positive rate better conforms with the significance level than the Wald test for low-SNR time series, as shown in Figure S-6. This LRT statistic is only for the Ricean AR(1) model, as the observed data loglikelihood is quite intractible for higher AR orders.[5] From standard results, the LRT statistic $\Lambda = 2[\ell(\widehat{\boldsymbol{\tau}}) - \ell(\tilde{\boldsymbol{\tau}})]$, where $\ell(\cdot)$ is the loglikelihood function $\log L(\cdot)$ and $\widehat{\boldsymbol{\tau}}$ and $\tilde{\boldsymbol{\tau}}$ represent the MLEs of $\boldsymbol{\tau}$ under H_a and H_0, respectively. Like the Wald statistic, the LRT statistic asymptotically follows a null χ^2_m-distribution. To derive the likelihood function $L(\boldsymbol{\tau}) = f(\boldsymbol{r}; \boldsymbol{\tau})$ for the Ricean AR(1) model, we note that $f(\boldsymbol{r}; \boldsymbol{\tau})$ can be factored as $f(r_1; \boldsymbol{\tau}) \prod_{t=2}^n f(r_t | r_{t-1}; \boldsymbol{\tau})$, where $f(r_1; \boldsymbol{\tau})$ is the Ricean PDF of (2). It can be shown (see Section S-2.4.2) that the conditional PDF $f(r_t | r_{t-1}; \boldsymbol{\tau})$ is equal to

$$\frac{r_t}{\sigma^2} e^{C_0} \left[\mathbb{I}_0\left(\frac{r_{t-1}\mu_{t-1}}{\gamma_0}\right)\right]^{-1} \sum_{m=0}^{\infty} \omega_m \mathbb{I}_m(C_1)\mathbb{I}_m(C_2)\mathbb{I}_m(C_{12}), \tag{12}$$

where $C_0 = -[r_t^2 + \mu_t^2 + \alpha^2(r_{t-1}^2 + \mu_{t-1}^2) - 2\alpha\mu_{t-1}\mu_t]/(2\sigma^2)$, $C_1 = r_{t-1}(\mu_{t-1} - \alpha\mu_t)/\sigma^2$, $C_2 = r_t(\mu_t - \alpha\mu_{t-1})/\sigma^2$, and $C_{12} = \alpha r_{t-1} r_t/\sigma^2$. Also, in (12), $\omega_m = 1$ for $m = 0$ and $\omega_m = 2$ for $m \geq 1$.

3.4. *Choosing the order of the AR model.* We suggest a sequential testing approach for determining the AR order p. Starting with $k = 1$, and for increasing k, we posit $H_0 : p = k - 1$ vs. $H_a : p \geq k$ (or, in terms of the AR coefficients, $H_0 : \forall j \geq k, \alpha_j = 0$ vs. $H_a : \exists j \geq k : \alpha_j \neq 0$). The estimated AR order is then

[5] Recall that the Wald test statistic can derived for any AR order.

$\widehat{p} = k' - 1$, where k' is the first k in the sequence of tests for which H_0 is not rejected. An LRT statistic given by $2(\ell_k - \ell_{k-1})$, where ℓ_k is the optimized loglikelihood function for the AR(k) model, may be employed under the CVS and MOG models. For the MOR model, we use the Wald test statistic $\widehat{\alpha}_k^2 / \mathscr{I}_e^{-1}(\widehat{\boldsymbol{\tau}}, \boldsymbol{r})_{\alpha_k \alpha_k}$, where the denominator is the diagonal entry of the inverse empirical information matrix corresponding to α_k. From standard results, each test statistic (whether LRT or Wald) is asymptotically χ_1^2-distributed under $H_0 : p = k - 1$.

It can be shown that the significance level δ applied to each test controls "over-detecting" the order (*i.e.*, $\widehat{p} > p$) in the sense that $\delta = \mathbb{P}(\widehat{p} > p | \widehat{p} \geq p)$. See Adrian, Maitra and Rowe (2018, Section S-2.4) for a justification. Section S-2.5 uses simulation to demonstrate that the sequential testing approach to detecting p gives similar results to approaches based on the AIC and BIC (Akaike, 1973; Schwarz, 1978).

Our development in this section has laid the groundwork for our investigation of fMRI analyses using the three models. We now proceed with our evaluations.

4. Simulation experiments. We perform simulation experiments to compare the AR(p) Ricean model to two other models in a setting of known truth. See Section 3.1 and Table 1 for a summary of these three models: the CV, MOR, and MOG models. We simulated low-SNR complex-valued time series under the CV model — and therefore also magnitude time series under the MOR model — with the $\boldsymbol{X}$ matrix of the finger-tapping experiment (see Section 2). We used white noise variance $\sigma^2 = 1$, AR(1) temporal dependence with AR parameters $\alpha = 0.2, 0.4, 0.6$, and 0.8, baseline signal levels β_0 from 0.5 to 5.0, and activation levels $\beta_1 = 0.1, 0.2$, and 0.3. Thus, the SNRs and CNRs of the simulated data corresponded with these in the dataset (see Figure S-3). For each combination of parameter values, we generated 10,000 voxel time series and fit each of the three models under an assumed AR order of 1. Our model comparison analysis has two main components: properties of the parameter estimates and activation detection performance. To quantify simulation variability, we calculated standard errors for all quantities using the bootstrap method (Efron and Tibshirani, 1986) with 1000 replications.

4.1. *Properties of parameter estimates.* Figure 2 summarizes the properties of the parameter estimates, displaying the biases, standard errors (SEs), and Root Mean Squared Errors (RMSEs) of $\widehat{\beta}_0$, $\widehat{\beta}_1$, $\widehat{\sigma}^2$, and $\widehat{\alpha}$. (It shows results for $\alpha = 0.4$; results for other αs are given in Figure S-9.) Focusing first on the biases, it is immediately evident that the MOG model produces the most biased parameter estimates due to its Gaussian approximation of the truly Ricean magnitudes. Specifically, the biases of $\widehat{\beta}_0$ and $\widehat{\sigma}^2$ result from the mean and variance of the Rice distribution (which are the quantities that the MOG model estimates) being above and below

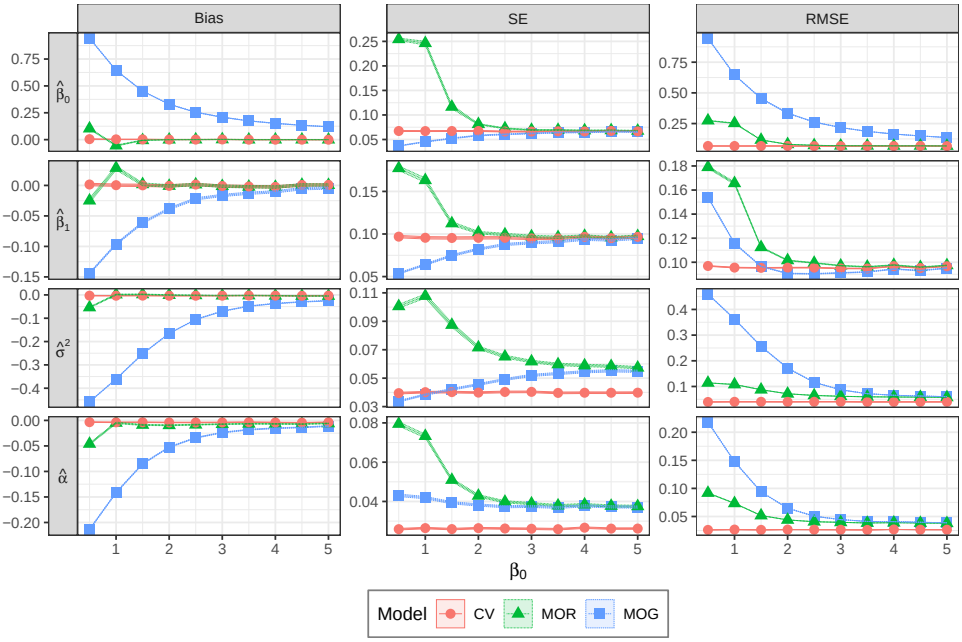

FIG 2. *Biases, SEs (SE), and RMSEs (RMSE) of* $\widehat{\beta}_0$, $\widehat{\beta}_1$, $\widehat{\sigma}^2$, *and* $\widehat{\alpha}$ *under three models for simulated time series under* $\beta_1 = 0.2$, $\alpha = 0.4$, *and different values of* β_0. *The shaded areas cover the estimate* $\pm$ *2 standard error intervals.*

the Ricean location and scale parameters (Zhu *et al.*, 2009). The MOG model biases decrease with increasing β_0 because the Gaussian approximation to the Rice distribution improves with SNR. These results match those already observed for the temporally independent case (Adrian, Maitra and Rowe, 2013; Solo and Noh, 2007), and, additionally, we see here that the MOG model-based estimate of the AR coefficient α is the most biased as well. The MOR model-based parameter estimates also show some biases at the lowest SNR time series; the CV model-based estimates are unbiased in all cases.

Switching our focus to the SEs, we note that the CV model-based SEs of $\widehat{\sigma}^2$ and $\widehat{\alpha}$ are lower than those for the MO models. This corresponds to a similar result observed in Rowe (2005b) about the sampling variances of $\widehat{\sigma}^2$ for the temporally independent case, and suggests that the *twice the quantities* feature of the CV data is driving this difference. Overall, the RMSEs, which account for both bias and SE as $\text{RMSE}^2(\cdot) = \text{Bias}^2(\cdot) + \text{SE}^2(\cdot)$, are lowest for the CV model; in addition, the CV model-based results are constant with β_0 — *i.e.,* not related to the SNR. This suggests that, provided the CV data is collected, the CV model produces the most reliable parameter estimates (arguing against the current practice of discarding the phase data). However, given that archival datasets (of which there are massively

many) do not have phase data stored, our results here also suggest the parameter estimation benefits of using the AR MOR model in place of the currently-used AR MOG model, especially in terms of bias for low SNR time series.

4.2. *Activation detection performance.* Next, we compare activation detection performance, calculating LRT statistics for the activation test of $H_0 : \beta_1 = 0$ vs. $H_a : \beta_1 \neq 0$ for each simulated time series. To summarize the power of each LRT statistic, we calculated the partial area under the receiver operating characteristic curve or the pAUC (McClish, 1989; Zhou, Obuchowski and McClish, 2011). The pAUC is the area under the ROC curve — where the ROC curve plots the true positive rate (TPR) against the false positive rate (FPR) — over a limited range of FPR values.[6] The rationale for using the pAUC rather than the (full) AUC, the area under the ROC curve for all FPR values from 0 to 1, is to exclude contributions to the curves from FPR values that are never used in practice, and to highlight differences between the methods in the part of the ROC that are most likely to be used in practice. For instance, using FPR values greater than 0.1 would allow for far too many false positives than practically ever used; indeed, our significance level threshold used on the real data in Section 5 is 0.001. Therefore, we calculated the pAUCs over a FPR range of 0 to 0.05. We calculated the pAUCs (separately for each combination of parameters β_0, β_1, and α) as the average of the TPRs for the significance levels $\delta = 0.0001, 0.0002, 0.0003, \ldots, 0.0500$; each TPR is the proportion of the 10,000 simulated test statistics greater than the $\chi^2_{1-\delta,1}$ quantile.

As shown in Figure 3, the pAUCs of simulated LRT statistics are consistently in the order (highest to lowest) of CV, MOR, and MOG models. While the figure shows between-panel differences in the pAUCs due to the relationships between the CNR and the values of β_1 and α (positive and negative relationships, respectively), the within-panel patterns are quite similar. While the CV model-based pAUCs are relatively constant as a function of β_0, the pAUCs of the two MO model-based LRTSs decrease with β_0.

We attribute the increased MOR model-based pAUCs relative to the MOG model to proper modeling of the Rice-distributed magnitudes: the MOG model resorts to a Gaussian approximation of the Rice distribution. Figure 4 displays the percent pAUC increases of the MOR model-based LRTSs relative to the MOG model. We note that the sizes of MOR model improvements in pAUC increase as β_0 and β_1 decrease and α increases, which correspond to decreases in SNR and CNR. While it is not surprising that a lower SNR (with worse Gaussian approximation of the Ricean magnitudes) is associated with a larger MOR model improvement, it is worth noting that improvement is larger for lower activation levels (CNRs) as well.

[6]There are also pAUC versions that limit the TPR range (or both the FPR and TPR ranges), but we use a FPR-limited pAUC here.

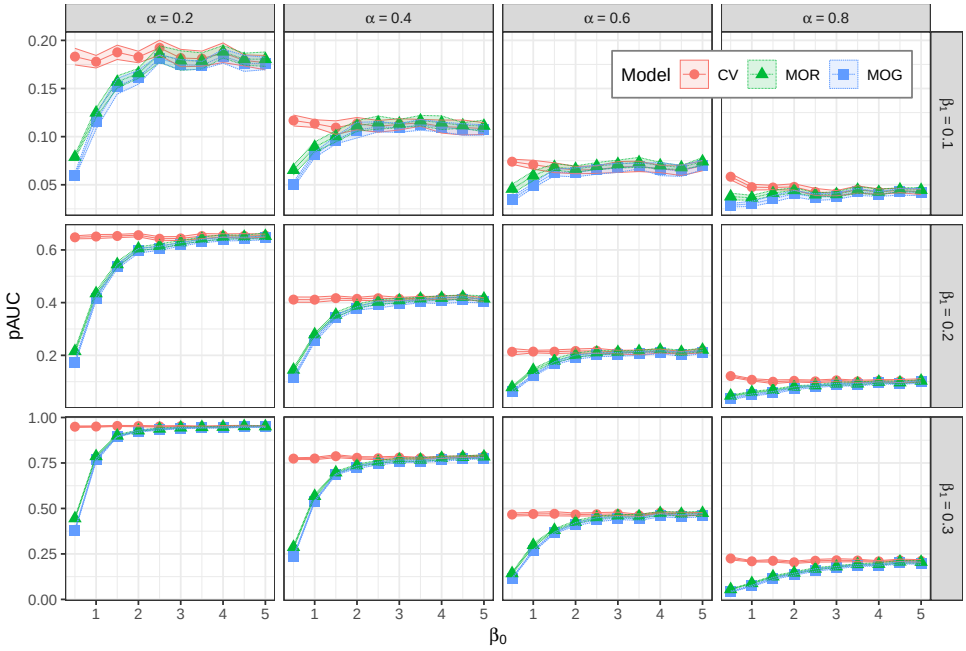

FIG 3. *The partial AUCs of the magnitude-only (MO) data-based LRT statistics decrease at low SNRs relative to their complex-valued (CV) data-based counterparts. Also, the Ricean (MOR) model-based pAUCs show improvements over those from the Gaussian (MOG) model. The shaded regions show the pAUCs* $\pm$ *2 standard errors.*

As for the CV versus MO comparison, the *twice the quantities* feature seems to be driving the difference in detection performance. The additional information in the phase data (again, which is usually not collected) appears to be more valuable to the activation detection as β_0 (the SNR) decreases, as shown by the increasing discrepancy in CV/MO pAUCs. In fact, we may view this in terms of the "missing information principle" (Orchard and Woodbury, 1972). Section S-3.1.1 describes how to calculate the observed (MO), missing (phase only), and complete (CV) data-based the Fisher information matrices by applying the EM algorithm. Interestingly, the curves of the "observed information" (in the MO data) and the "complete information" (in the CV data) in Figure 5 look similar to the MO and CV model-based pAUC curves in Figure 3. Both figures suggest that the phase data contain useful information about the activation, even though the activation itself occurs in the magnitude signal $\boldsymbol{X}\boldsymbol{\beta}$.

To summarize, the results of our experiments suggest that modeling the *Ricean magnitudes* produces less-biased parameter estimates and better activation detection performance than the Gaussian approximation. Also, using *twice the quantities* in CV rather than MO data-based models leads to parameter estimates with

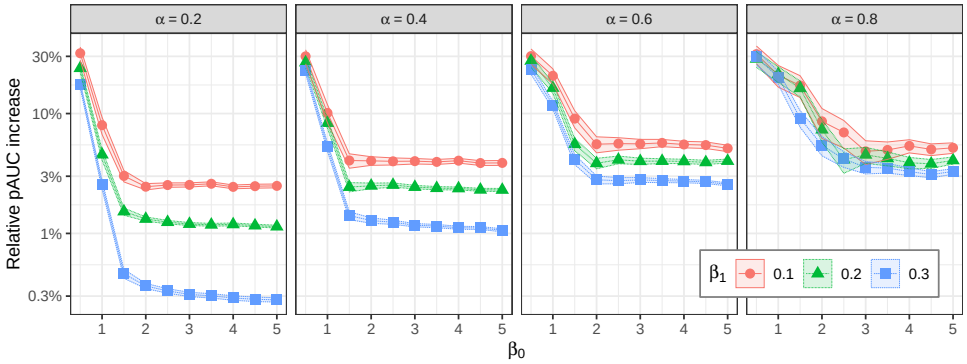

FIG 4. *Relative improvement in MOG model-based pAUCs by MOR model, that is, (MOR - MOG) / MOG. Shaded areas show estimate ± 2 standard errors.*

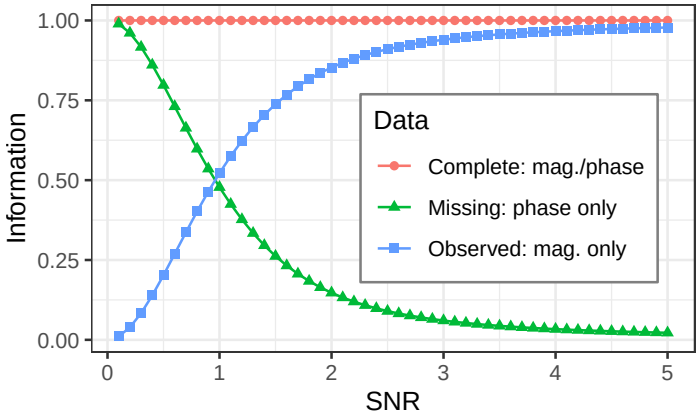

FIG 5. *Plots of the information matrices as a function of the SNR.*

less variation and additionally improved activation detection. Although using the CV data produces the best estimation and activation detection, the CV data has historically not been collected; in this case, utilizing the Ricean model when only magnitude (archival) data is available produces sizeable gains over the Gaussian approximation.

5. Results on low-signal fMRI dataset. In this section, we identify activation in the low-SNR fMRI dataset introduced in Section 2 under the CV, MOR, and MOG models. Working with each voxel time series of the dataset separately, we first detected the AR orders (see Figure S-10) and then tested for activation using $H_0 : \beta_1 = 0$ vs. $H_a : \beta_1 \neq 0$, obtaining p-values from the LR and Wald

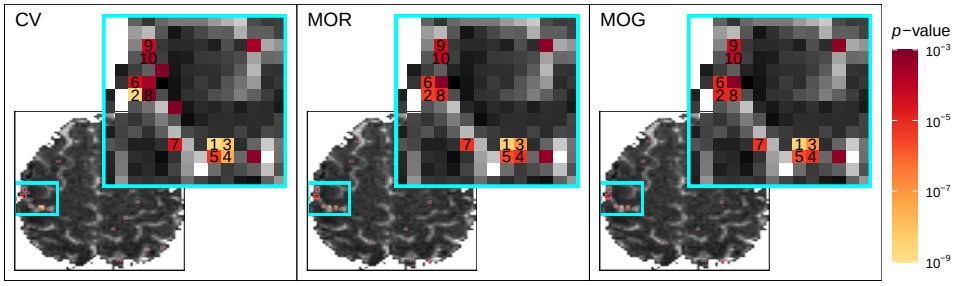

FIG 6. *Activation maps with inset maps showing left central sulcus ROI; numbered voxels represent those having test statistics with the lowest p-values.*

test statistics under the null χ^2_1-distribution. To determine activation, we used a significance level threshold of 0.001 (Woo, Krishnan and Wager, 2014).

5.1. *Activation detection in raw data.* We display activation maps of the second slice[7] according to each of the three models in Figure 6. Each map shows a

	Voxel numbers from Fig. 6										
Model	1	2	3	4	5	6	7	8	9	10	avg
CV	8.82	8.70	8.18	7.53	5.31	4.42	4.65	3.14	4.24	3.61	5.86
MOR	8.48	5.52	6.93	5.20	5.71	5.21	5.20	5.00	4.37	4.13	5.57
MOG	8.49	4.96	6.94	5.20	5.71	5.03	5.21	5.00	4.37	4.13	5.50

TABLE 2

Negative logarithm (base 10) of the p-values for the voxels numbered 1-10 in the inset maps of Figure 6 for test statistics under the CV, MOR, and MOG models. (For instance, the CV model-based p-value for voxel 1 is $10^{-8.82}$*.) Also, the "avg" column represents the average across voxels.*

grayscale anatomical image (the magnitude image at the first time point) with the voxels having p-values less than 0.001 colored according to the legend. The activation is rather sparse except for a region containing the left central sulcus (Figure 1) — recall, the site guiding right-hand function for normal healthy adults — so we focus on this region of interest (ROI) in the inset maps. Specifically, we focus on the ten voxels in this ROI with test statistics that provide the lowest minimum p-value over the three models, which are identified by numerals (from 1 = lowest to 10 = highest p-value) in the inset maps of Figure 6. This numbering carries over to Table 2 where the size of the p-values can be compared more clearly across models. (See Figure S-12 for a graphical representation of Table 2.) Though this comparison varies of across voxels, we note that the average of the log base-10 p-values is lowest for the CV model, followed by the MOR model and then by the MOG model. As we saw in simulation experiments, the experimental data also indicates

[7]We focus on the second slice (in the superior direction) because it shows the strongest activation. For comparison with the two neighboring slices, see Figure S-11.

that if the CV data is available, the CV model produces better activation detection power than MO data-based models. However, in the common case of MO data, our AR(p) Ricean model shows more power than the the corresponding model based on a Gaussian approximation to the Rice distribution.

5.2. *Adding noise to the raw data.* To further investigate the effect that low SNR has on activation detection, we added more noise to the acquired CV data. So, for the ten voxels identified in Figure 6 with acquired CV time series (y_{Rt}, y_{It}), $t = 1, \ldots, 621$, we obtained new synthetic data $y^*_{Rt} = y_{Rt} + w_{Rt}$ and $y^*_{It} = y_{It} + w_{It}$, with $w_{Rt}, w_{It} \sim$ iid $N(0, \sigma_a^2)$. Because a representative, data-based estimate of the noise SD is 0.15, we generated data using $\sigma_a = 0.15, 0.20, 0.25$, and 0.30. Adding noise to the original data in this manner reduces the SNR and CNR (see Figure S-13) as would occur with increasing spatial resolution or decreasing field strength of the MR scan. Table 3 shows the proportions of the 10,000 generated datasets in which each of the ten voxels was detected under each model at the 0.001 significance level (also see Figure S-14). With the added noise, the detection power more consistently follows the order of CV (greatest), MOR, and MOG (least) models across the 10 voxels than the p-values of the raw data in Figure 6.

6. Discussion. In this paper, we developed a Ricean model for fMRI magnitude time series that incorporates autoregressive time dependence. Our approach applies AR(p) errors to the Gaussian-distributed real and imaginary components from which the magnitudes are computed. We estimated model parameters from the MO data using the EM algorithm with the phase portion of the latent complex-valued data playing the role of missing data. We then extended the EM algorithm to derive Wald and LRTs for activation and AR order detection.

We compared this AR(p) Ricean model to two other models: the CV model for complex-valued data and the MOG model which employs a Gaussian approximation for the truly Rice-distributed magnitudes. As previously discussed, complex-valued fMRI data is rarely collected in practice (although we strongly advocate for it); so, our main focus is how to make the best use of existing (*i.e.*, archived) magnitude-only data through the MOR rather than the MOG model. We expected the CV model to perform better than the two MO data-based models simply due to the CV data having *twice the quantities* and the MOR model to perform better than the MOG model due to properly modeling the *Ricean magnitudes*.

Simulation-based results confirmed these expectations when we evaluated the quality of parameter estimates and the activation detection under each model. The parameter estimates of the CV model had lower RMSEs than the MO data-based models, and the MOR model-based parameter estimates were much less biased than those from the MOG model. Similarly, we demonstrated greater activation detection power (as measured by pAUC) for the CV model than the two MO data-

		SD of added noise σ_a			
Voxel	Model	0.15	0.2	0.25	0.3
1	CV	0.951 (0.002)	0.731 (0.004)	0.476 (0.005)	0.304 (0.004)
1	MOR	0.931 (0.002)	0.670 (0.004)	0.390 (0.004)	0.216 (0.004)
1	MOG	0.903 (0.003)	0.625 (0.004)	0.363 (0.004)	0.200 (0.004)
2	CV	0.947 (0.002)	0.719 (0.004)	0.479 (0.005)	0.306 (0.004)
2	MOR	0.929 (0.002)	0.660 (0.004)	0.409 (0.004)	0.230 (0.004)
2	MOG	0.868 (0.003)	0.579 (0.005)	0.357 (0.004)	0.204 (0.004)
3	CV	0.896 (0.003)	0.633 (0.004)	0.399 (0.004)	0.238 (0.004)
3	MOR	0.717 (0.004)	0.398 (0.004)	0.212 (0.004)	0.103 (0.003)
3	MOG	0.718 (0.004)	0.405 (0.004)	0.209 (0.004)	0.102 (0.003)
4	CV	0.880 (0.003)	0.611 (0.004)	0.378 (0.004)	0.229 (0.004)
4	MOR	0.408 (0.004)	0.180 (0.004)	0.090 (0.003)	0.045 (0.002)
4	MOG	0.351 (0.004)	0.156 (0.003)	0.081 (0.002)	0.042 (0.002)
5	CV	0.490 (0.005)	0.261 (0.004)	0.152 (0.003)	0.090 (0.003)
5	MOR	0.513 (0.005)	0.244 (0.004)	0.121 (0.003)	0.057 (0.002)
5	MOG	0.442 (0.005)	0.210 (0.004)	0.106 (0.003)	0.052 (0.002)
6	CV	0.811 (0.004)	0.525 (0.005)	0.314 (0.004)	0.192 (0.004)
6	MOR	0.788 (0.004)	0.468 (0.005)	0.242 (0.004)	0.132 (0.003)
6	MOG	0.629 (0.004)	0.357 (0.004)	0.188 (0.004)	0.108 (0.003)
7	CV	0.361 (0.004)	0.187 (0.004)	0.109 (0.003)	0.068 (0.002)
7	MOR	0.412 (0.004)	0.201 (0.004)	0.108 (0.003)	0.060 (0.002)
7	MOG	0.372 (0.004)	0.187 (0.004)	0.102 (0.003)	0.057 (0.002)
8	CV	0.443 (0.005)	0.240 (0.004)	0.133 (0.003)	0.085 (0.003)
8	MOR	0.410 (0.004)	0.214 (0.004)	0.108 (0.003)	0.065 (0.002)
8	MOG	0.322 (0.004)	0.171 (0.003)	0.091 (0.003)	0.057 (0.002)
9	CV	0.293 (0.004)	0.165 (0.003)	0.085 (0.003)	0.058 (0.002)
9	MOR	0.282 (0.004)	0.143 (0.003)	0.068 (0.002)	0.038 (0.002)
9	MOG	0.283 (0.004)	0.142 (0.003)	0.067 (0.002)	0.039 (0.002)
10	CV	0.193 (0.004)	0.109 (0.003)	0.067 (0.002)	0.042 (0.002)
10	MOR	0.216 (0.004)	0.109 (0.003)	0.054 (0.002)	0.028 (0.002)
10	MOG	0.182 (0.004)	0.093 (0.003)	0.048 (0.002)	0.025 (0.001)
avg	CV	0.627 (0.001)	0.418 (0.001)	0.259 (0.001)	0.161 (0.001)
avg	MOR	0.561 (0.001)	0.329 (0.001)	0.180 (0.001)	0.097 (0.001)
avg	MOG	0.507 (0.001)	0.293 (0.001)	0.161 (0.001)	0.089 (0.001)

TABLE 3

Proportions (and their standard errors) of simulated time series detected as detected when noise with standard deviation σ_a was added to the raw data for the 10 voxels identified in Figure 6. The "avg" rows show average proportions over the 10 voxels.

based models, and the MOR model-based pAUCs were greater than those from the MOG model. For all comparisons, the differences were greatest at low SNRs.

We then compared these models on a finger-tapping experiment, acquiring the data using the body coil to study a low-SNR dataset. For voxels in the expected activation region showing the most activation, the CV model produced the lowest average p-values, followed by the MOR model (and the MOG model last). Although the order of the p-values varied by voxel, we are able to more consistently superior activation detection of the CV model (and MOR model greater than MOG model) when we added extra simulated white noise to the experimental voxel time series, which decreased the SNR.

A reviewer has asked about the computational complexity of MO Ricean over CV data-based methods. We note that while the CV-based analysis has a larger

storage requirement, the CV-based and Gaussian MO models are of lower computs can use direct methods to estimate parameters, the CV-based analysis is the highest since it deals with twice the amount of data, however, in terms of CPU usage, CV-based analysis (and Gaussian MO-only analysis) have lower computational complexity than the Rice-based model. However, the Rice-based MO analysis is more accurate, in terms of parameter estimation and activation detaction, than the Gaussian MO-only analysis, and especially at lower SNR.

Future directions for this research can explore fMRI time series models that allow for activation in magnitude and phase (Rowe, 2005a). The models we have focused upon in this article (even the CV data-based ones) have assumed task-related changes in magnitude only, with no task-related phase changes. It may be worth exploring a single model that allows for both. Another area for future work lies in generalizing the modeling of magnitude time series beyond the AR(p) Rice model presented here. MR images collected by simultaneous acquisition from multiple independent coils (Tristán-Vega, Aja-Fernández and Westin, 2012) can be shown to follow the non-central chi distribution, with degrees of freedom equal to twice the number of coils (Wegmann, Eklund and Villani, 2017). The Rice distribution is the special case for a single coil and two degrees of freedom.

Acknowledgents. We thank the Editor, an anonymous Associate Editor and an anonymous reviewer whose comments on a earlier version of this paper greatly improved its content and presentation.

REFERENCES

ABDI, A., TEPEDELENLIOGLU, C., KAVEH, M. and GIANNAKIS, G. (2001). On the estimation of the K parameter for the Rice fading distribution. *IEEE Communications Letters* **5** 92-94.

ABRAMOWITZ, M. and STEGUN, I. (1965). *Handbook of Mathematical Functions*. Dover Publications.

ADRIAN, D. W., MAITRA, R. and ROWE, D. B. (2013). Ricean over Gaussian modeling in magnitude fMRI analysis – Added complexity with neglible practical benefits. *Stat* **2** 303-316.

ADRIAN, D. W., MAITRA, R. and ROWE, D. B. (2018). Complex-valued time series modeling for improved activation detection in fMRI studies. *Annals of Applied Statistics* **12** 1451-1478.

AITKIN, M. and AITKIN, I. (1996). A hybrid EM/Gauss-Newton algorithm for maximum likelihood in mixture distributions. *Statistics and Computing* **6** 127-130.

AKAIKE, H. (1973). *2nd International Symposium on Information Theory* Information theory and an extension of the maximum likelihood principle 267-281. Akademiai Kiado.

ARAFA, A. and MESSIER, G. G. (2010). A Gaussian Model for Dead-Reckoning Mobile Sensor Position Error. In *2010 IEEE 72nd Vehicular Technology Conference - Fall* 1-5.

BAÏLE, R., MUZY, J.-F. and POGGI, P. An M-Rice wind speed frequency distribution. *Wind Energy* **14** 735-748.

BALCHANDANI, P. and NAIDICH, T. P. (2015). Ultra-High-Field MR Neuroimaging. *American Journal of Neuroradiology* **36** 1204-1215.

BANDETTINI, P. A., JESMANOWICZ, A., WONG, E. C. and HYDE, J. S. (1993). Processing strategies for time-course data sets in functional MRI of the human brain. *Magnetic Resonance in Medicine* **30** 161-173.

BAR-SHALOM, Y., LI, X. R. and KIRUBARAJAN, T. (2001). *Estimation with applications to tracking and navigation: theory algorithms and software*. John Wiley & Sons.

BELLIVEAU, J. W., KENNEDY, D. N., MCKINSTRY, R. C., BUCHBINDER, B. R., WEISSKOFF, R. M., COHEN, M. S., VEVEA, J. M., BRADY, T. J. and ROSEN, B. R. (1991). Functional mapping of the human visual cortex by magnetic resonance imaging. *Science* **254** 716-719.

BEST, D. J., RAYNER, J. C. W. and THAS, O. (2010). Easily applied tests of fit for the Rayleigh distribution. *Sankhya, Series B* **72** 254–263.

BROWN, T. R., KINCAID, B. M. and UGURBIL, K. (1982). NMR chemical shift imaging in three dimensions. In *Proceedings of the National Academy of Sciences, USA* **79** 3523-3526.

BULLMORE, E., BRAMMER, M., WILLIAMS, S. C. R., RABE-HESKETH, S., JANOT, N., DAVID, A., MELLERS, J., HOWARD, R. and SHAM, P. (1996). Statistical methods of estimation and inference for function MR image analysis. *Magnetic Resonance in Medicine* **35** 261-277.

CARPENTER, M. B. (1991). *Core Text of Neuroanatomy*. Williams and Wilkins.

CASELLA, G. and BERGER, R. L. (2002). *Statistical Inference*, Second edition ed. Thomson Learning.

COSOTTINI, M. and ROCCATAGLIATA, L. (2021). Neuroimaging at 7 T: are we ready for clinical transition? *European Radiology Experimental* **5** 37.

DEMPSTER, A. P., LAIRD, N. M. and RUBIN, D. (1977). Maximum likelihood from incomplete data via the EM algorithm. *Journal of Royal Statistical Society Series B* **23** 1-38.

DEN DEKKER, A. J., POOT, D. H. J., BOS, R. and SIJBERS, J. (2009). Likelihood-based hypothesis tests for brain activation detection from MRI data disturbed by colored noise: a simulation study. *IEEE Transactions on Medical Imaging* **28** 287-296.

EFRON, B. and TIBSHIRANI, R. (1986). Bootstrap Methods for Standard Errors, Confidence Intervals, and Other Measures of Statistical Accuracy. *Statistical Science* **1** 54 – 75. Available at https://doi.org/10.1214/ss/1177013815

FRISTON, K. J., JEZZARD, P. and TURNER, R. (1994). Analysis of functional MRI time-series. *Human Brain Mapping* **1** 153-171.

FRISTON, K. J., FRITH, C. D., LIDDLE, P. F., DOLAN, R. J., LAMMERTSMA, A. A. and FRACKOWIAK, R. S. J. (1990). The relationship between global and local changes in PET scans. *Journal of Cerebral Blood Flow and Metabolism* **10** 458-466.

FRISTON, K. J., HOLMES, A. P., WORSLEY, K. J., POLINE, J.-B., FRITH, C. D. and FRACKOWIAK, R. S. J. (1995). Statistical parametric maps in functional imaging: A general linear approach. *Human Brain Mapping* **2** 189-210.

FRISTON, K. J., JOSEPHS, O., ZARAHN, E., HOLMES, A. P., ROUQETTE, S. and POLINE, J.-B. (2000). To smooth or not to smooth? Bias and efficiency in fMRI time-series analysis. *NeuroImage* **12** 196-208.

GENOVESE, C. R., LAZAR, N. A. and NICHOLS, T. E. (2002). Thresholding of statistical maps in functional neuroimaging using the false discovery rate:. *NeuroImage* **15** 870-878.

GLISSON, T. H. (2011). *Introduction to Circuit Analysis and Design*. Springer, The Netherlands.

GLOVER, G. H. (1999). Deconvolution of impulse response in event-related BOLD fMRI. *NeuroImage* **9** 416-429.

GUDBJARTSSON, H. and PATZ, S. (1995). The Rician distribution of noisy data. *Magnetic Resonance in Medicine* **34** 910-914.

HAHN, A. D., NENCKA, A. S. and ROWE, D. B. (2009). Improving robustness and reliability of phase-sensitive fMRI analysis using temporal off-resonance alignment of single-echo timeseries (TOAST). *NeuroImage* **44** 742-752.

HAHN, A. D., NENCKA, A. S. and ROWE, D. B. (2012). Enhancing the Utility of Complex-

Valued Functional Magnetic Resonance Imaging Detection of Neurobiological Processes Through Postacquisition Estimation and Correction of Dynamic B_0 Errors and Motion. *Human Brain Mapping* **33** 288-306.

HAJRI, N., YOUSSEF, N. and PATZOLD, M. (2009). A study on the statistical properties of double hoyt fading channels. In *2009 6th International Symposium on Wireless Communication Systems* 201-205.

HENKELMAN, R. M. (1985). Measurement of signal intensities in the presence of noise in MR images. *Medical Physics* **12** 232-233.

ISLAM, K. T., ZHONG, S., ZAKAVI, P., CHEN, Z., KAVNOUDIAS, H., FARQUHARSON, S., DURBRIDGE, G., BARTH, M., MCMAHON, K. L., PARIZEL, P. M., DWYER, A., EGAN, G. F., LAW, M. and CHEN, Z. (2023). Improving portable low-field MRI image quality through image-to-image translation using paired low- and high-field images. *Scientific Reports* **13**.

JAIN, A. K. (1989). *Fundaments of Digital Image Processing*. Prentice Hall.

JESMANOWICZ, A., WONG, E. C. and HYDE, J. S. (1993). Phase Correction for EPI Using Internal Reference Lines. In *Proceedings from the International Society of Magnetic Resonance in Medicine* **12** 1239.

JEZZARD, P. and CLARE, S. (2001). Principles of nuclear magnetic resonance and MRI. In *Functional MRI: An Introduction to Methods* (P. Jezzard, P. M. Matthews and S. M. Smith, eds.) 3 67-92. Oxford University Press.

KUMAR, A., WELTI, D. and ERNST, R. R. (1975). NMR Fourier Zeugmatography. *Journal of Magnetic Resonance* **18** 69-83.

KWONG, K. K., BELLIVEAU, J. W., CHESLER, D. A., GOLDBERG, I. E., WEISSKOFF, R. M., PONCELET, B. P., KENNEDY, D. N., HOPPEL, B. E., COHEN, M. S., TURNER, R., CHENG, H.-M., BRADY, T. J. and ROSEN, B. R. (1992). Dynamic Magnetic Resonance Imaging of Human Brain Activity During Primary Sensory Stimulation. *Proceedings of the National Academy of Sciences of the United States of America* **89** 5675-5679.

LAZAR, N. A. (2008). *The Statistical Analysis of Functional MRI Data*. Springer.

LEE, C. C., JACK, C. R. and RIEDERER, S. J. (1998). Mapping of the Central Sulcus with Functional MR: Active versus Passive Activation Tasks. *American Journal of Neuroradiology* **19** 847-852.

LEE, C. C., WARD, H. A., SHARBROUGH, F. W., MEYER, F. B., MARSH, W. R., RAFFEL, C., SO, E. L., CASCINO, G. D., SHIN, C., XU, Y., RIEDERER, S. J. and JACK, C. R. (1999). Assessment of Functional MR Imaging in Neurosurgical Planning. *American Journal of Neuroradiology* **20** 1511-1519.

LINDSEY, W. (1964). Error probabilities for Rician fading multichannel reception of binary and n-ary signals. *IEEE Transactions on Information Theory* **10** 339-350.

LIU, Y., LEONG, A. T. L., ZHAO, Y., XIAO, L., MAK, H. K. F., TSANG, A. C. O., LAU, G. K. K., LEUNG, G. K. K. and WU, E. X. (2021). A low-cost and shielding-free ultra-low-field brain MRI scanner. *Nature Communications* **12** 1-14. Available at https://doi.org/10.1038/s41467-021-27317-1

LJUNGGREN, S. (1983). A Simple Graphical Representation of Fourier-Based Imaging Methods. *Journal of Magnetic Resonance* **54** 338-343.

LOCASCIO, J. J., JENNINGS, P. J., MOORE, C. I. and CORKIN, S. (1997). Time series analysis in the time domain and resampling methods for studies of functional magnetic resonance brain imaging. *Human Brain Mapping* **5** 168-193.

LOGAN, B. R. and ROWE, D. B. (2004). An evaluation of thresholding techniques in fMRI analysis. *NeuroImage* **22** 95-108.

MACOVSKI, A. (1996). Noise in MRI. *Magnetic Resonance in Medicine* **36** 494-497.

MARCHINI, J. L. and RIPLEY, B. D. (2000). A new statistical approach to detecting significant activation in functional MRI. *NeuroImage* **12** 366-380.

MCCLISH, D. K. (1989). Analyzing a Portion of the ROC Curve. *Medical Decision Making* **9** 190-195. Available at https://pubmed.ncbi.nlm.nih.gov/2668680/

MCLACHLAN, G. J. and KRISHNAN, T. (2008). *The EM Algorithm and Extensions*. Wiley.

MEILIJSON, I. (1989). A fast improvement to the EM algorithm on its own terms. *Journal of the Royal Statistical Society. Series B (Methodological)* **51** 127-138.

MENG, X.-L. and RUBIN, D. B. (1993). Maximum likelihood estimation via the ECM algorithm: a general framework. *Biometrika* **80** 267-278.

MILLER, J. W. (1995). Exact Maximum Likelihood Estimation in Autoregressive Processes. *Journal of Time Series Analysis* **16** 607-615.

MURPHY, K., BODURKA, J. and BANDETTINI, P. A. (2007). How long to scan? The relationship between fMRI temporal signal to noise ratio and necessary scan duration. *Neuroimage* **34** 565-574.

NENCKA, A. S., HAHN, A. D. and ROWE, D. B. (2008). The Use of Three Navigator Echoes in Cartesian EPI Reconstruction Reduces Nyquist Ghosting. In *Proceedings from the International Society of Magnetic Resonance in Medicine* **16** 3032.

OGAWA, S., LEE, T. M., NAYAK, A. S. and GLYNN, P. (1990). Oxygenation-sensitive contrast in magnetic resonance image of rodent brain at high magnetic fields. *Magnetic Resonance in Medicine* **14** 68-78.

ORCHARD, T. and WOODBURY, M. A. (1972). A missing information principle: theory and applications. In *Proceedings of the Sixth Berkeley Symposium on Mathematical Statistics and Probability* **1** 697-715. University of California Press, Berkeley, California.

POURAHMADI, M. (2001). *Foundations of Time Series Analysis and Prediction Theory*. Wiley.

POWERS, J. M., IOACHIM, G. and STROMAN, P. W. (2018). Ten Key Insights into the Use of Spinal Cord fMRI. *Brain Sciences* **8** 173.

RICE, S. O. (1944). Mathematical analysis of random noise. *Bell Systems Technical Journal* **23** 282.

ROSEN, B. R. and SAVOY, R. L. (2012). fMRI at 20: Has it changed the world? *NeuroImage*.

ROWE, D. B. (2005a). Modeling both the magnitude and phase of complex-valued fMRI data. *NeuroImage* **25** 1310-1324.

ROWE, D. B. (2005b). Parameter estimation in the magnitude-only and complex-valued fMRI data models. *NeuroImage* **25** 1124-1132.

ROWE, D. B. (2016). *Handbook of Neuroimaging Data Analysis* Image Reconstruction in Functional MRI 205-232. Chapman & Hall/CRC.

ROWE, D. B. and LOGAN, B. R. (2004). A complex way to compute fMRI activation. *NeuroImage* **23** 1078-1092.

RUMEAU, C., TZOURIO, N., MURAYAMA, N., PERETTI-VITON, P., LEVRIER, O., JOLIOT, M., MAZOYER, B. and SALAMON, G. (1994). Location of Hand Function in the Sensorimotor Cortex: MR and Functional Correlation. *American Journal of Neuroradiology* **15** 567-572.

SCHWARZ, G. E. (1978). Estimating the dimension of a model. *Annals of Statistics* **6** 461-464.

SIJBERS, J., DEN DEKKER, A. J., SCHEUNDERS, P. and DYCK, D. V. (1998). Maximum-Likelihood Estimation of Rician Distribution Parameters. *IEEE Transactions on Medical Imaging* **17** 357-361.

SOLO, V. and NOH, J. (2007). An EM algorithm for Rician fMRI activation detection. In *ISBI* 464-467.

TRISTÁN-VEGA, A., AJA-FERNÁNDEZ, S. and WESTIN, C.-F. (2012). Least squares for diffusion tensor estimation revisited: Propagation of uncertainty with Rician and non-Rician signals. *NeuroImage* **59** 4032-4043. Copyright - Copyright Elsevier Limited Feb 15, 2012; Last updated - 2016-11-01. Available at http://search.proquest.com.ezproxy.gvsu.edu/docview/1834299434?accountid=39473

TWEIG, D. B. (1983). The k-trajectory formulation of the NMR imaging process with applications in analysis and synthesis of imaging methods. *Medical Physics* **10** 610-21.

WANG, T. and LEI, T. (1994). Statistical analysis of MR imaging and its applications in image modeling. *Proceedings of the IEEE International Conference on Image Processing and Neural Networks* **1** 866-870.

WANG, Y., HU, Q., LI, L., FOLEY, A. M. and SRINIVASAN, D. (2019). Approaches to wind power curve modeling: A review and discussion. *Renewable and Sustainable Energy Reviews* **116** 109422. Available at https://doi.org/10.1016/j.rser.2019.109422

WEGMANN, B., EKLUND, A. and VILLANI, M. (2017). Bayesian Rician Regression for Neuroimaging. *Frontiers in Neuroscience* **11**.

WOO, C.-W., KRISHNAN, A. and WAGER, T. D. (2014). Cluster-extent based thresholding in fMRI analyses. *NeuroImage* **91** 412-419.

WORSLEY, K. J., MARRETT, S., NEELIN, P., VANDAL, A. C., FRISTON, K. J. and EVANS, A. C. (1996). A unified statistical approach for determining significant voxels in images of cerebral activation. *Human Brain Mapping* **4** 58-73.

YU, C.-H., PRADO, R., OMBAO, H. and ROWE, D. (2018). A Bayesian Variable Selection Approach Yields Improved Detection of Brain Activation from Complex-Valued fMRI. *Journal of the American Statistical Association* **113** 1395-1410.

ZHANG, J. L., RUSINEK, H., CHANDARANA, H. and LEE, V. S. (2013). Functional MRI of the kidneys. *Journal of Magnetic Resonance Imaging* **37** 282-293.

ZHOU, X. H., OBUCHOWSKI, N. A. and MCCLISH, D. K. (2011). *Statistical methods in diagnostic medicine*, Second edition ed. Wiley.

ZHU, H., LI, Y., IBRAHIM, J. G., SHI, X., AN, H., CHEN, Y., GAO, W., LIN, W., ROWE, D. B. and PETERSON, B. S. (2009). Regression Models for Identifying Noise Sources in Magnetic Resonance Images. *Journal of the American Statistical Association* **104** 623-637.

(2024). Improving probabilistic wind speed forecasting using M-Rice distribution and spatial data integration. *Applied Energy* **360** 122840.

DEPARTMENT OF STATISTICS
GRAND VALLEY STATE UNIVERSITY
ALLENDALE, MI 49401-9403
USA
E-MAIL: adriad1@gvsu.edu

DEPARTMENT OF STATISTICS
IOWA STATE UNIVERSITY
AMES, IA 50011-1090
USA
E-MAIL: maitra@iastate.edu

DEPARTMENT OF MATHEMATICAL AND STATISTICAL SCIENCES
MARQUETTE UNIVERSITY
MILWAUKEE, WI 53233
USA
E-MAIL: daniel.rowe@marquette.edu

Submitted to the Annals of Applied Statistics

SUPPLEMENT TO "RICE-DISTRIBUTED AUTOREGRESSIVE TIME SERIES MODELING OF MAGNITUDE FUNCTIONAL MRI DATA"

BY DANIEL W. ADRIAN[‡] AND RANJAN MAITRA[*,§] AND DANIEL B. ROWE[†,¶]

Grand Valley State University[‡] and Iowa State University[§] and Marquette University[¶]

S-1. Supplement to Section 2 – Further description of the dataset. Figure S-1 shows plots of the real, imaginary, magnitude, and phase time series at a single voxel, at one of the voxels showing the most activation. It also displays the time course of the "on-off" fingertapping and the expected BOLD response obtained by convolving this 0/1 stimulus time course with the Glover (1999) hemodynamic response function (HRF). Although this BOLD response is present in the data, trends in the time series (also known as also scanner drift) are also present which must be accounted for.

S-1.1. *Detrending scanner drift.* Detrending scanner drift is a common preprocessing step in the statistical analysis of fMRI time series. Two sources of this drift are noise from the MR scanner and aliasing of cardiorespiratory cycles (Tanabe *et al.*, 2002), and the magnitude of these changes "often far exceeds" both the white noise and the amplitude of the task-related single change (Genovese, 2000). Our study of the dataset's time series suggests diverse, nonlinear shapes of drift profiles, not only for magnitude time series such as those reported in Genovese (2000), but for the real, imaginary, and phase time series as well. Figure S-2 shows the plot of such a time series and compares four methods for fitting the trend: the CV running line (Adrian, Maitra and Rowe, 2018), a polynomial fit, a natural cubic spline, and a smoothing spline. We determined that the smoothing spline was the preferred choice, but to study the robustness of our choice, we used both the CV running line and smoothing splines in practice.[1] Figure S-2 shows a plot of the magnitude and phase time series for a selected voxel and compares the fit from four curve fitting methods. One is the "CV running line" method introduced in Adrian, Maitra and Rowe (2018) that fits linear models to both the magnitude and phase time series (simultaneously), using a moving window that only considers

[*]Research supported in part by the the National Science Foundation CAREER Grant # DMS-0437555 and the National Institutes of Health (NIH) awards #R21EB016212 and #R21EB034184.

[†]Research supported in part by the National Institutes of Health (NIH) award #R21NS087450.

[1]Indeed, the results were very similar for both detrending approaches, so we only present those based on smoothing splines.

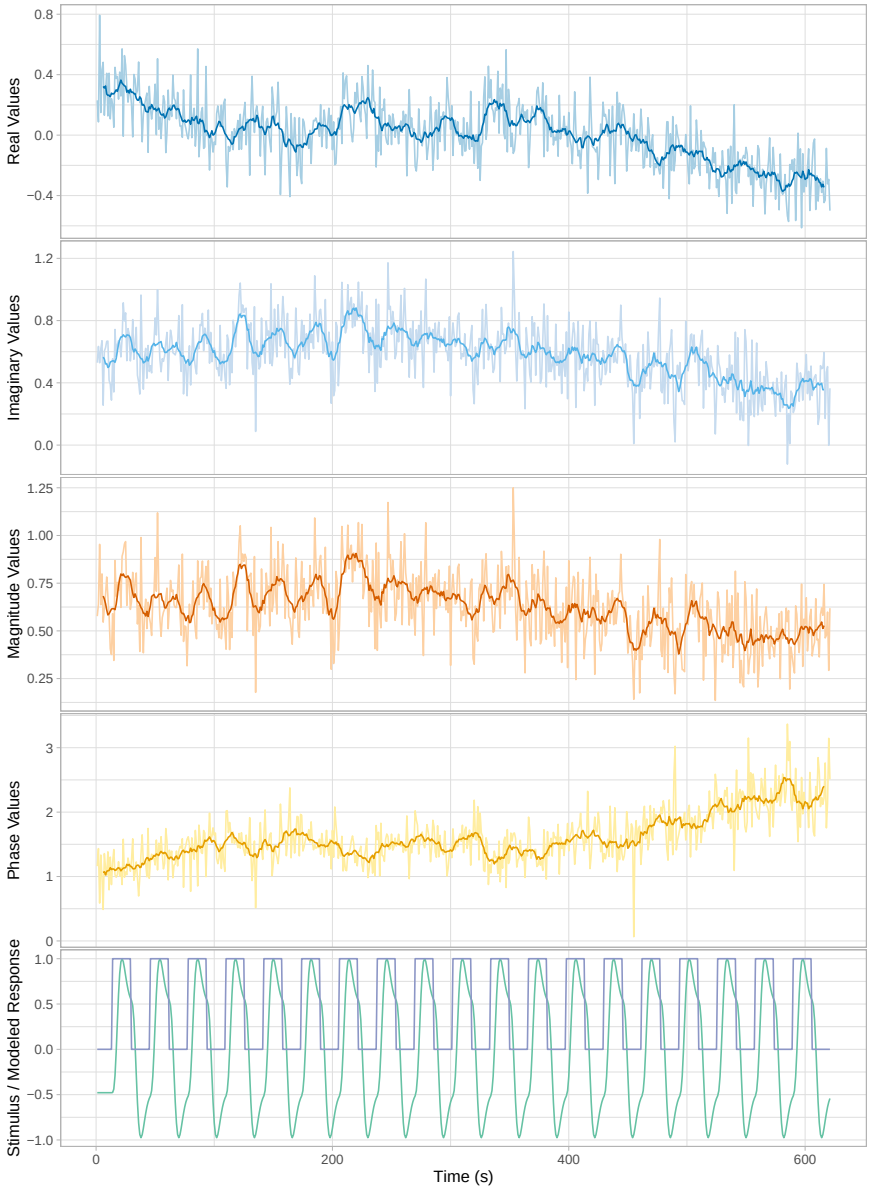

FIG S-1. *Time series of (from top) the real, imaginary, magnitude, and phase observations for one of the voxels showing the most activation. Lighter lines in each display represents the raw time series, while the darker lines show the result after applying a simple, central moving average filter with 5 nearest neighbors. The bottom display is of the 0/1 block design of the stimulus superimposed with the stimulus/HRF convolution, after zero-centering and unit scaling.*

time points within 64 seconds of the fitted time. The other three are more established curve-fitting methods: a polynomial of degree 8, a natural cubic spline with

6 evenly spaced knots, and a smoothing spline with 8 effective degrees of freedom (Hastie, Tibshirani and Friedman, 2009). These last three methods are all based on fitting separate curves to the real and the imaginary time series. As shown in

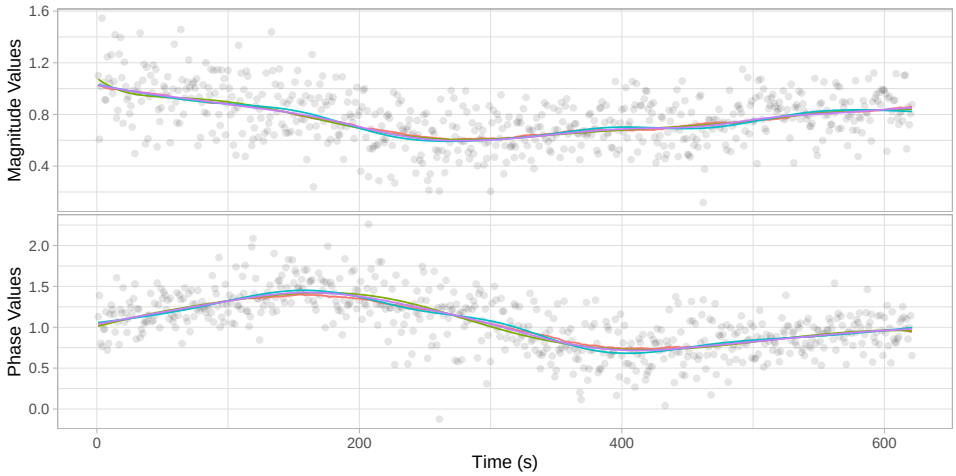

(a) Raw data and fitted curves shown

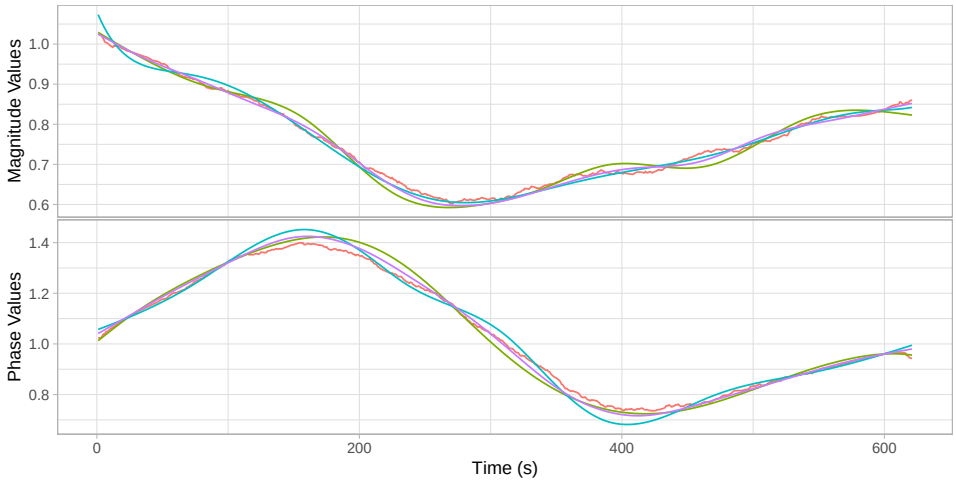

(b) Only fitted curves shown

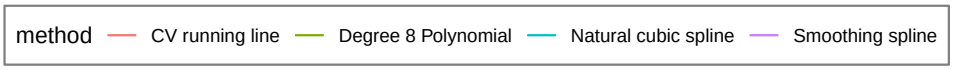

FIG S-2. *Comparison of four curve fitting methods on a selected voxel's time series for the purpose of detrending to correct scanner drift: CV running line (Adrian, Maitra and Rowe, 2018), degree 8 polynomial, natural cubic spline with 6 evenly spaced knots, smoothing spline with 8 effective degrees of freedom.*

Figure S-2(a), the four methods all capture changes in the global nonlinear trend well. However, a closer look in Figure S-2(b) shows some differences. For one, the

CV running line does not produce a smooth curve, which may introduce additional variance to the detrended time series. Overall, it appears that the smoothing spline is the "Goldilocks' choice" as it seems to do the best in terms of not taking the largest or smallest fitted value across all time points for both time series.

For clarity, we describe the detrending process using notation. First, for the real and imaginary data, y_{Rt} and y_{It}, at a single voxel and time t, we use one of the four methods to obtain the fitted trend values $\widehat{y}_{Rt}$ and $\widehat{y}_{It}$. The detrended values are then calculated as $\breve{y}_{\xi t} = y_{\xi t} - \widehat{y}_{\xi t} + \bar{\widehat{y}}_{\xi}$, for $\xi = R, I$, where $\bar{\widehat{y}}_{\xi}$ is the mean of the fitted values across the corresponding time series. (The same approach applied to magnitude-only data produces the magnitude-only detrended data.)

S-1.2. *Graphical summaries of SNR and CNR.* Figure S-3 shows spatial and frequency distributions of the signal-to-noise ratio (SNR) and the contrast-to-noise ratio (CNR) of the dataset. The SNRs and CNRs above were calculated as $\widehat{\beta}_0/\widehat{\sigma}$

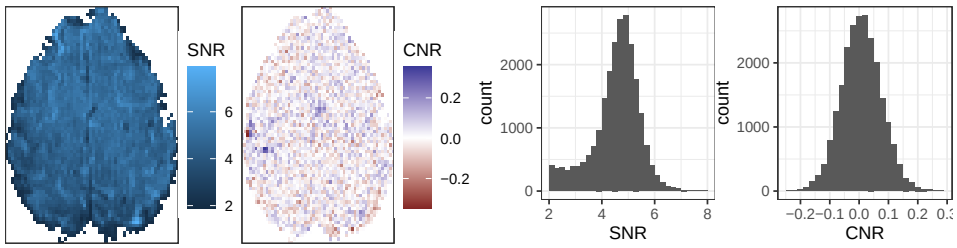

FIG S-3. *Graphical summaries of SNR and CNR: (left) images of slice 2; (right) frequency distributions*

and $\widehat{\beta}_1/\widehat{\sigma}$, respectively, where the previous parameter estimates were calculated from the magnitude voxel time series using ordinary least squares regression with an intercept term and the expected BOLD response in Figure S-1.

S-2. Supplement to Section 3 – Further Methodological Development.

S-2.1. *CV and MOG model methodology.*

S-2.1.1. *CV model.* The log-likelihood function is given by

$$\log f(\boldsymbol{y}_R, \boldsymbol{y}_I; \boldsymbol{\tau}) = -n \log \sigma^2 - \log |\boldsymbol{R}_n| - h/(2\sigma^2), \tag{S-1}$$

where

$$h = \begin{pmatrix} \boldsymbol{y}_R - \boldsymbol{X}\boldsymbol{\beta}\cos\theta \\ \boldsymbol{y}_I - \boldsymbol{X}\boldsymbol{\beta}\sin\theta \end{pmatrix}' \begin{pmatrix} \boldsymbol{R}_n^{-1} & 0 \\ 0 & \boldsymbol{R}_n^{-1} \end{pmatrix} \begin{pmatrix} \boldsymbol{y}_R - \boldsymbol{X}\boldsymbol{\beta}\cos\theta \\ \boldsymbol{y}_I - \boldsymbol{X}\boldsymbol{\beta}\sin\theta \end{pmatrix}. \tag{S-2}$$

The maximum likelihood estimate (MLE) of $\boldsymbol{\beta}$ is $\widehat{\boldsymbol{\beta}} = \widehat{\boldsymbol{\beta}}_R \cos\widehat{\theta} + \widehat{\boldsymbol{\beta}}_I \sin\widehat{\theta}$, where $\widehat{\boldsymbol{\beta}}_R = (\boldsymbol{X}'\widehat{\boldsymbol{R}}_n^{-1}\boldsymbol{X})^{-1}\boldsymbol{X}'\widehat{\boldsymbol{R}}_n^{-1}\boldsymbol{y}_R$, $\widehat{\boldsymbol{\beta}}_I = (\boldsymbol{X}'\widehat{\boldsymbol{R}}_n^{-1}\boldsymbol{X})^{-1}\boldsymbol{X}'\widehat{\boldsymbol{R}}_n^{-1}\boldsymbol{y}_I$, and $\widehat{\boldsymbol{R}}_n^{-1}$ is a

function of $\widehat{\boldsymbol{\alpha}}$, the MLE of $\boldsymbol{\alpha}$, according to the $(2p+1)$-diagonal matrix given in Pourahmadi (2001). Further, the MLEs of θ and σ^2 are given by

$$\widehat{\theta} = \frac{1}{2}\arctan\left[\frac{2\widehat{\boldsymbol{\beta}}_R'\boldsymbol{X}'\widehat{\boldsymbol{R}}_n^{-1}\boldsymbol{X}\widehat{\boldsymbol{\beta}}_I}{\widehat{\boldsymbol{\beta}}_R'\boldsymbol{X}'\widehat{\boldsymbol{R}}_n^{-1}\boldsymbol{X}\widehat{\boldsymbol{\beta}}_R - \widehat{\boldsymbol{\beta}}_I'\boldsymbol{X}'\widehat{\boldsymbol{R}}_n^{-1}\boldsymbol{X}\widehat{\boldsymbol{\beta}}_I}\right] \tag{S-3}$$

and $\widehat{\sigma}^2 = \widehat{h}/(2n)$, where $\widehat{h}$ evaluates the parameters in (S-2) at their MLEs. We obtain $\widehat{\boldsymbol{\alpha}}$ by solving the system of equations (Miller, 1995)

$$\widehat{d}_{0k} = \sum_{j=1}^{p}(\widehat{d}_{jk} + 2j\widehat{\gamma}_{|j-k|})\widehat{\alpha}_j, \tag{S-4}$$

for $k = 1, \ldots, p$, with $\widehat{d}_{ij} = \sum_{t=1}^{n-i-j}\widehat{\eta}_{R,t+i}\widehat{\eta}_{R,t+j} + \widehat{\eta}_{I,t+i}\widehat{\eta}_{I,t+j}$, $0 \le i, j \le p$, and $\widehat{\gamma}_k = \widehat{d}_{0k}/(2n)$, wherein $\widehat{\eta}_{Rt} = y_{Rt} - \boldsymbol{x}_t'\widehat{\boldsymbol{\beta}}\cos\widehat{\theta}$ and $\widehat{\eta}_{It} = y_{It} - \boldsymbol{x}_t'\widehat{\boldsymbol{\beta}}\sin\widehat{\theta}$, $t = 1, \ldots, n$. In practice, ML estimation consists of alternately updating $(\widehat{\theta}, \widehat{\boldsymbol{\beta}})$ and $(\widehat{\boldsymbol{\alpha}}, \widehat{\boldsymbol{R}}_n^{-1})$ in a Cochrane and Orcutt (1949)-type procedure until convergence. The LRT statistic for the test of $H_0 : \boldsymbol{C}\boldsymbol{\beta} = \boldsymbol{0}$ vs. $H_a : \boldsymbol{C}\boldsymbol{\beta} \neq \boldsymbol{0}$ is given by

$$\Lambda_{CVS,p} = 2n\log\left(\frac{\tilde{\sigma}^2}{\widehat{\sigma}^2}\right) - 2\log\left(\left|\tilde{\boldsymbol{R}}_p^{-1}\right| / \left|\widehat{\boldsymbol{R}}_p^{-1}\right|\right), \tag{S-5}$$

where $\boldsymbol{R}_p$ is such that $\sigma^2\boldsymbol{R}_p = \mathrm{Cov}(\eta_{R1}, \ldots, \eta_{Rp}) = \mathrm{Cov}(\eta_{I1}, \ldots, \eta_{Ip})$, $\boldsymbol{R}_p^{-1}$ is a function of $\boldsymbol{\alpha}$ as in Pourahmadi (2001), and the "hats" and "tildes" denote quantities maximized with respect to H_a and H_0, respectively. It can be shown that $\Lambda_{CVS,p}$ follows an asymptotic χ^2_m null distribution, where $m = \mathrm{rank}(\boldsymbol{C})$.

S-2.1.2. *MOG model.* The log-likelihood function for the MOG model is given by $\log f(\boldsymbol{r};\boldsymbol{\tau}) = -\frac{n}{2}\log\sigma^2 - \frac{1}{2}\log|\boldsymbol{R}_n| - \frac{1}{2\sigma^2}(\boldsymbol{r} - \boldsymbol{X}\boldsymbol{\beta})'\boldsymbol{R}_n^{-1}(\boldsymbol{r} - \boldsymbol{X}\boldsymbol{\beta})$, where $\boldsymbol{R}_n$ is such that $\sigma^2\boldsymbol{R}_n = \mathrm{Cov}(\boldsymbol{\epsilon})$. The MLEs of $\boldsymbol{\beta}$ and σ^2 are given by $\widehat{\boldsymbol{\beta}} = (\boldsymbol{X}'\widehat{\boldsymbol{R}}_n^{-1}\boldsymbol{X})^{-1}\boldsymbol{X}'\widehat{\boldsymbol{R}}_n^{-1}\boldsymbol{r}$ and $\widehat{\sigma}^2 = (\boldsymbol{r} - \boldsymbol{X}\widehat{\boldsymbol{\beta}})'\widehat{\boldsymbol{R}}_n^{-1}(\boldsymbol{r} - \boldsymbol{X}\widehat{\boldsymbol{\beta}})/n$, respectively. We obtain $\widehat{\boldsymbol{\alpha}}$ by solving the system of equations $\sum_{j=1}^{p}\{\widehat{d}_{ij} + (j/n)\widehat{d}_{0,|i-j|}\}\widehat{\alpha}_j = \widehat{d}_{0i}$, $i = 1, \ldots, p$, where $\widehat{d}_{ij} = \sum_{t=1}^{n-i-j}\widehat{\epsilon}_{t+i}\widehat{\epsilon}_{t+j}$, for $0 \le i, j \le p$, and $\widehat{\epsilon}_t = r_t - \boldsymbol{x}_t'\widehat{\boldsymbol{\beta}}$, $t = 1, \ldots, n$. The estimation procedure begins with $\widehat{\boldsymbol{R}}_n = \boldsymbol{I}_n$ and then iteratively updates $\widehat{\boldsymbol{\beta}}$, $\widehat{\boldsymbol{\alpha}}$, and $\widehat{\boldsymbol{R}}_n^{-1}$ until convergence. The LRT statistic for the test of $H_0 : \boldsymbol{C}\boldsymbol{\beta} = \boldsymbol{0}$ vs. $H_a : \boldsymbol{C}\boldsymbol{\beta} \neq \boldsymbol{0}$ is given by

$$\Lambda_{MOG,p} = n\log(\tilde{\sigma}^2/\widehat{\sigma}^2) - \log\left(\left|\tilde{\boldsymbol{R}}_p^{-1}\right| / \left|\widehat{\boldsymbol{R}}_p^{-1}\right|\right), \tag{S-6}$$

where $\boldsymbol{R}_p$ is such that $\sigma^2\boldsymbol{R}_p = \mathrm{Cov}(\epsilon_1, \ldots, \epsilon_p)$.

S-2.2. *Relationships between CV, MOR, and MOG model densities.* We illustrate some relationships between the probability density functions (PDFs) of the CV, MOR, and MOG models for the observations at a single voxel and time-point. Before we get into the derivations, let us state these relationships:

1. **Fact 1**: The MOR model PDF is the marginal PDF for the magnitude in the CV model PDF.
2. **Fact 2**: For large SNR, the MOR model PDF approaches the MOG model PDF.

Derivation of Fact 1. Under the CV model (and suppressing subscripts for time), the PDF is

(S-7)
$$f(y_R, y_I; \mu, \gamma_0, \theta) = (2\pi\gamma_0)^{-1} \exp\left[-\frac{(y_R - \mu\cos\theta)^2 + (y_I - \mu\sin\theta)^2}{2\gamma_0}\right].$$

Transforming this PDF for the real/imaginary data to the magnitude/phase data yields

$$f(r, \phi; \mu, \gamma_0, \theta) = \frac{r}{2\pi\gamma_0} \exp\left[\frac{-(r^2+\mu^2)}{2\gamma_0}\right] \exp\left[\frac{\mu r}{\gamma_0}\cos(\phi - \theta)\right]. \tag{S-8}$$

The MO Ricean PDF then arises from integrating out ϕ in (S-8). That is, because $\int_{-\pi}^{\pi} \exp[\mu r \gamma_0 \cos(\phi - \theta)] d\phi = 2\pi \mathbb{I}_0(\mu r/\gamma_0)$, the Ricean PDF (Rice, 1944) is

$$f(r; \mu, \gamma_0) = \frac{r}{\gamma_0} \exp\left[\frac{-(r^2+\mu^2)}{2\gamma_0}\right] \mathbb{I}_0\left(\frac{\mu r}{\gamma_0}\right). \tag{S-9}$$

Derivation of Fact 2. It can be shown the Ricean PDF approaches the Gaussian PDF at large SNRs – that is, for large values of $\mu/\sqrt{\gamma_0}$. We use the approximation (Abramowitz and Stegun, 1965) that for large values of x,

$$\mathbb{I}_0(x) = (2\pi x)^{-1/2} e^x \{1 + 1/(8x) + \mathcal{O}(x^{-2})\}. \tag{S-10}$$

Thus, for large SNR, which also implies large values of $\mu r/\gamma_0$, substituting (S-10) into the Ricean PDF (S-9) yields the Gaussian PDF

$$f(r; \mu, \gamma_0) = (2\pi\gamma_0)^{-1/2} \exp[-(r-\mu)^2/(2\gamma_0)] \tag{S-11}$$

times two additional terms, $(r/\mu)^{1/2}$ and $[1+(1/8)(\mu r/\gamma_0)^{-1}]$ that approach unity for large SNRs. (The former approaches unity because $|r - \mu|$ is on the order of $\sqrt{\gamma_0} \ll \mu_t$.) Indeed, Figure S-4 shows that the Ricean and Gaussian PDFs converge with increasing SNR.

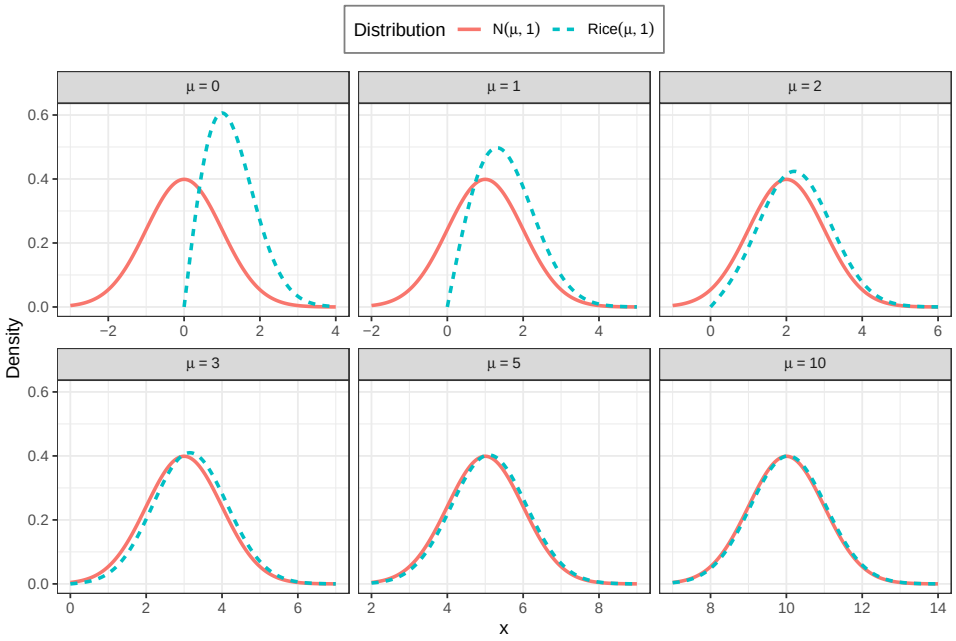

FIG S-4. *As the SNR (here, μ) increases, the Ricean and Gaussian PDFs converge.*

S-2.3. *Supplement to Section 3.2.1 – Methodological details of the EM algorithm corresponding to the AR(p) Ricean model.*

S-2.3.1. *Supplement to Section 3.2.1 – Univariate Expectations.* To find the univariate expectations $\mathbb{E}_{\phi_t|r_t;\boldsymbol{\tau}^{(k)}}[\cos(\phi_t - \theta)]$, we show that the distribution of ϕ_t conditional on r_t is von Mises. From standard results, the conditional PDF $f(\phi_t|r_t;\boldsymbol{\tau})$ is the joint PDF $f(\phi_t, r_t;\boldsymbol{\tau})$ in (S-8) divided by the marginal PDF $f(r_t;\boldsymbol{\tau})$ in (S-9). Thus, the conditional PDF is

$$f(\phi_t|r_t;\boldsymbol{\tau}) = \left[2\pi\mathbb{I}_0\left(\frac{\mu_t r_t}{\gamma_0}\right)\right]^{-1} \exp\left[\frac{\mu_t r_t}{\gamma_0}\cos(\phi_t - \theta)\right], \tag{S-12}$$

which is the von Mises PDF with location parameter θ and concentration parameter $\mu_t r_t/\gamma_0$ (Mardia and Jupp, 2000). It then follows from properties of the von Mises distribution that the univariate expectations $\mathbb{E}_{\phi_t|r_t;\boldsymbol{\tau}^{(k)}}[\cos(\phi_t - \theta)] = \mathbb{A}(r_t\mu_t^{(k)}/\gamma_0^{(k)})$, $t = 1, \ldots, n$.

S-2.3.2. *Supplement to Section 3.2.1 – Bivariate Expectations.* Here, we show that the bivariate expectations $\mathbb{E}[\cos(\phi_t - \phi_{t+j})|r_t, r_{t+j}, \boldsymbol{\tau}^{(k)}]$ can be reduced to the univariate expectations in (5). Our strategy is to take the bivariate expectation as the "iterated expectations" $\mathbb{E}_{\phi_t|r_t}[\mathbb{E}_{\phi_{t+j}|\phi_t,r_t,r_{t+j}}\{\cos(\phi_{t+j} - \phi_t)\}]$. First, expanding

the cosine term yields

$$\mathbb{E}_{\phi_t|r_t}\Big\{\cos(\phi_t-\theta)\mathbb{E}_{\phi_{t+j}|\phi_t,r_t,r_{t+j}}[\cos(\phi_{t+j}-\theta)] + \sin(\phi_t-\theta)\mathbb{E}_{\phi_{t+j}|\phi_t,r_t,r_{t+j}}[\sin(\phi_{t+j}-\theta)]\Big\}. \tag{S-13}$$

We now derive the conditional PDF of ϕ_{t+j} given ϕ_t, r_t, r_{t+j}. Starting with the distributions of $(y_{Rt}, y_{R,t+j})$ and $(y_{It}, y_{I,t+j})$, which are independent and bivariate normal, and using its magnitude and phase transformations, it can be shown that

$$f(\phi_{t+j}|\phi_t, r_t, r_{t+j}) \propto \exp[\kappa\cos(\phi_{t+j}-\theta) + \delta\cos(\phi_{t+j}-\phi_t)], \tag{S-14}$$

where $\kappa = r_{t+j}(\gamma_0\mu_{t+j} - \gamma_j\mu_t)/b$ and $\delta = \gamma_j r_t r_{t+j}/b$, with $b = \gamma_0^2 - \gamma_j^2$. It can then be shown that $\phi_{t+j}|\phi_t, r_t, r_{t+j}$ follows the von Mises distribution by writing the bracketed portion of (S-14) as $K\cos(\phi_{t+j}-\Psi)$ where $K = [\kappa^2 + \delta^2 + 2\kappa\delta\cos(\phi_t-\theta)]^{1/2}$ and Ψ is such that $\sin(\Psi-\theta) = \delta\sin(\phi_t-\theta)/K$ and $\cos(\Psi-\theta) = [\kappa+\delta\cos(\phi_t-\theta)]/K$. Thus, the conditional distribution of $(\phi_{t+j}-\theta)$ given ϕ_t, r_t, r_{t+j} is von Mises with location parameter $\Psi-\theta$ and concentration parameter K. It follows that $E_{\phi_{t+j}|\phi_t,r_t,r_{t+j}}[\cos(\phi_{t+j}-\theta)] = A(K)\cos(\Psi-\theta)$ and $E_{\phi_{t+j}|\phi_t,r_t,r_{t+j}}[\sin(\phi_{t+j}-\theta)] = A(K)\sin(\Psi-\theta)$ (Mardia and Jupp, 2000). Substituting these expectations into (S-13) and using the earlier expressions for the sine and cosine of $(\Psi-\theta)$, we obtain (5).

S-2.3.3. *Supplement to Section 3.2.1 – Maximizing with respect to constraints.* To find $\boldsymbol{\beta}^{(k+1)} = \text{argmax}_{\boldsymbol{\beta}}\, Q(\boldsymbol{\alpha}^{(k+1)}, \boldsymbol{\beta}, \sigma^{2(k)}; \boldsymbol{\tau}^{(k)})$ as part of the (conditional) M-step, we must maximize with respect to the constraint $\boldsymbol{X}\boldsymbol{\beta}^{(k+1)} \geq \mathbf{0}$. In the following, we illustrate this constrained maximization for the $\boldsymbol{X}$ matrix defined in Section 2.2, which has two columns: the first is an intercept containing all ones and the second is the expected BOLD response, which we denote by $\boldsymbol{b}$. It can be shown that $\boldsymbol{X}\boldsymbol{\beta} \geq \mathbf{0}$ if and only if $\boldsymbol{A}\boldsymbol{\beta} \geq \mathbf{0}$, where $\boldsymbol{A}$ contains only two rows of $\boldsymbol{X}$: the rows $\boldsymbol{a}_1' = (1, \min(\boldsymbol{b}))$ and $\boldsymbol{a}_2' = (1, \max(\boldsymbol{b}))$. To maximize with respect to $\boldsymbol{A}\boldsymbol{\beta} \geq \mathbf{0}$, we first calculate the unrestricted maximizer

$$\widehat{\boldsymbol{\beta}} = (\boldsymbol{X}'\boldsymbol{R}_n^{-1}\boldsymbol{X})^{-1}\boldsymbol{X}'\boldsymbol{R}_n^{-1}\boldsymbol{u}^{(k)}. \tag{S-15}$$

If $\boldsymbol{A}\widehat{\boldsymbol{\beta}} \geq \mathbf{0}$, then $\boldsymbol{\beta}^{(k+1)} = \widehat{\boldsymbol{\beta}}$. Otherwise, let $J = \{j : \boldsymbol{a}_j'\widehat{\boldsymbol{\beta}} < 0\}$. Calculate $\tilde{\boldsymbol{\beta}}_j = \boldsymbol{\Omega}_j\widehat{\boldsymbol{\beta}}$ for each $j \in J$, where $\boldsymbol{\Omega}_j = \boldsymbol{I}_2 - [\boldsymbol{a}_j'(\boldsymbol{X}'\boldsymbol{R}_n^{-1}\boldsymbol{X})^{-1}\boldsymbol{a}_j]^{-1}(\boldsymbol{X}'\boldsymbol{R}_n^{-1}\boldsymbol{X})^{-1}\boldsymbol{a}_j\boldsymbol{a}_j'$. Then $\boldsymbol{\beta}^{(k+1)}$ is the $\tilde{\boldsymbol{\beta}}_j$ which maximizes $Q(\boldsymbol{\alpha}^{(k+1)}, \tilde{\boldsymbol{\beta}}_j, \sigma^{2(k)}; \boldsymbol{\tau}^{(k)})$.

S-2.3.4. *Supplement to Section 3.2.2 – Empirical Information Matrix.* We illustrate the calculation of $\boldsymbol{s}(r_t; \boldsymbol{\tau})$, $t = p+1, \ldots, n$, the contributions to the score

statistic from time t from which the empirical information matrix $\mathscr{I}_e(\boldsymbol{\tau};\boldsymbol{r})$ is constructed as in (10). We denote the elements of $\boldsymbol{s}(r_t;\boldsymbol{\tau})$ that come from taking the partial derivatives in (9) with respect to σ^2, $\boldsymbol{\alpha}$, and $\boldsymbol{\beta}$ by $s_{\sigma^2}(t)$, $\boldsymbol{s}_{\boldsymbol{\alpha}}(t)$, and $\boldsymbol{s}_{\boldsymbol{\beta}}(t)$, respectively. It can be shown that $s_{\sigma^2}(t) = [\tilde{\boldsymbol{\alpha}}'\boldsymbol{D}_t\tilde{\boldsymbol{\alpha}} - 2\sigma^2]/(2\sigma^4)$, where $\boldsymbol{D}_t$ is a matrix of order $(p+1)$ having (i,j)th entry $d_t(i,j) = r_{t-i}r_{t-j}E_{t-i,t-j} - \mu_{t-i}u_{t-j} - \mu_{t-j}u_{t-i} + \mu_{t-i}\mu_{t-j}$, $0 \le i,j \le p$, with $E_{rs} = \mathbb{E}_{\boldsymbol{\phi}|\boldsymbol{r};\boldsymbol{\tau}}[\cos(\phi_r - \phi_s)]$, $u_t = r_t A(r_t\mu_t/\gamma_0)$, and $\mu_t = \boldsymbol{x}_t'\boldsymbol{\beta}$. Further, $\boldsymbol{s}_{\boldsymbol{\alpha}}(t) = \boldsymbol{D}'_{t(0)}\tilde{\boldsymbol{\alpha}}/\sigma^2$, where $\boldsymbol{D}_{t(0)}$ is the matrix $\boldsymbol{D}_t$, but without the first row. Finally, $\boldsymbol{s}_{\boldsymbol{\beta}}(t) = \tilde{\boldsymbol{\alpha}}'\boldsymbol{D}_{t,\boldsymbol{\beta}}\tilde{\boldsymbol{\alpha}}/(2\sigma^2)$, where $\boldsymbol{D}_{t,\boldsymbol{\beta}}$ is the partial derivative of $\boldsymbol{D}_t$ with respect to $\boldsymbol{\beta}$, with (i,j)th entry $d_{t,\boldsymbol{\beta}}(i,j) = (u_{t-i} - \mu_{t-i})\boldsymbol{x}_{t-j} + (u_{t-j} - \mu_{t-j})\boldsymbol{x}_{t-i}$.

S-2.3.5. *Supplement to Section 3.2.2 – Computation time.* The computation time under the MOR model is much greater than the other models because the convergence of the EM algorithm is slow, even with the acceleration provided by the hybrid scheme including Newton-Raphson steps. Figure S-5 shows the computation times required for parameter estimation of 1000 simulated time series under

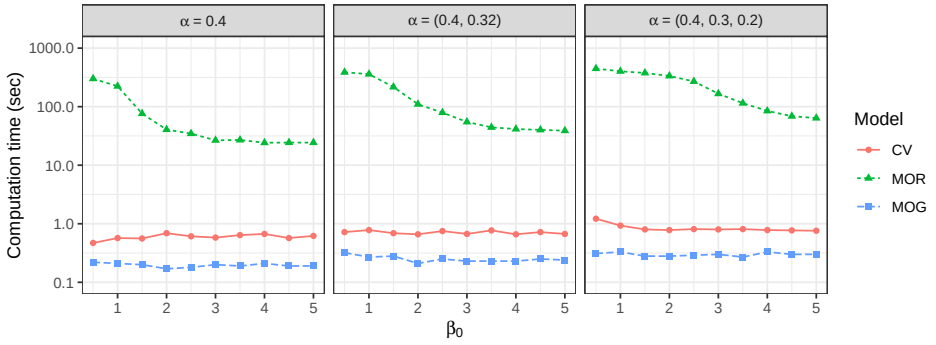

FIG S-5. *Computation times (sec) for parameter estimation per 1000 simulated time series under the three models. The EM algorithm used by the MOR model has much slower convergence than the other estimation schemes.*

the three models. We generated these time series under the CV model with $\boldsymbol{X}$ matrix described in Section 2.2, $\sigma^2 = 1$, $\boldsymbol{\beta} = (\beta_0, 0)'$ for β_0 from 0.5 to 5.0, and AR coefficients of 0.4, $(0.4, 0.32)$, and $(0.4, 0.3, 0.2)$. In our calculation, we assumed the correct AR order was known. Per thousand time series, the computation times for MOR model range from 24 to 447 seconds, while the other models are most always under one second. It is interesting to note that the MOR model computation time decreases as the SNR increases, decreasing by a factor of 10 as β_0 increases from 0.5 to 5.0. Computation times also increase for all models as the AR order increases.

S-2.4. *Supplement to Section 3.3 – Further details regarding test statistics.*

S-2.4.1. *Supplement to Section 3.3 – Comparing false positive rates.* The following simulation experiment examines the basic utility of the Wald and likelihood ratio test (LRT) statistics in terms of whether they follow their theoretical null distributions. To mimic the finger-tapping experiment, we generated magnitude time series from the AR(1) Ricean model with the two-column $\boldsymbol{X}$ matrix described in Section 2. Of the parameter $\boldsymbol{\beta} = (\beta_0, \beta_1)$ corresponding to $\boldsymbol{X}$, only β_1 is activation-related; thus, the activation test is $H_0 : \beta_1 = 0$ vs. $H_a : \beta_1 \neq 0$, and we set $\beta_1 = 0$ to examine the null distributions of the test statistics, which theoretically should be χ^2_1. To examine an SNR range similar to that in the dataset (see Figure S-3), we set $\sigma = 1$ and varied β_0 from 0.5 to 5.0. We set $\alpha_1 = 0.3$, generated 10,000 time series for each β_0 value, and calculated the Wald and LRT statistics. Figure S-6 shows the proportions of test statistics in which H_0 was rejected (in effect,

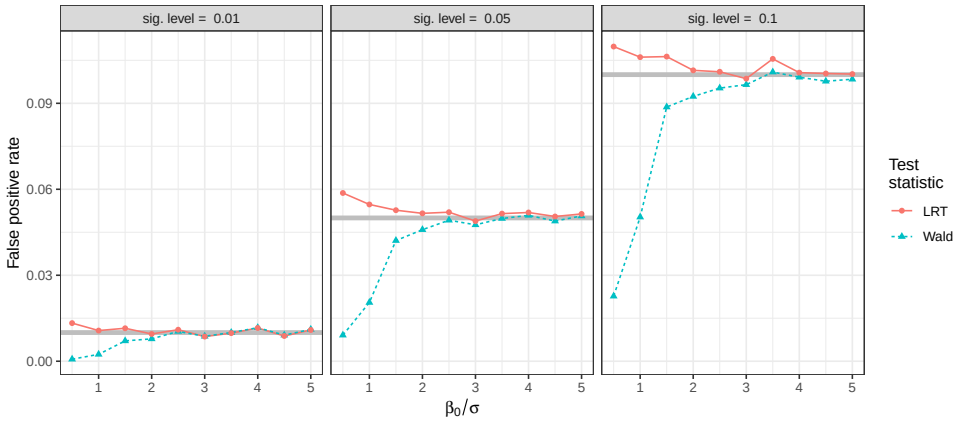

FIG S-6. *The false positive rates of the Wald test statistics fall sharply below the significance levels (shown by the thick grey lines) for β_0/σ values below 2, showing that LRT statistic is more reliable for low SNRs.*

the false positive rates) based on the theoretical χ^2_1 null distribution at significance levels of 0.01, 0.05, and 0.10. If the test statistic truly followed the theoretical null distribution, each false positive rate should be close to the significance level (with small discrepancies explained by simulation variability). However, it is evident that the Wald test is unusable at β_0 values below 2 due to its false positive rates falling sharply below the significance level. Overall, the LRT statistic seems more reliable due to its false positive rates better conforming with the significance level.

S-2.4.2. *Supplement to Section 3.3 – Ricean AR(1) LRT statistic.* Here, we derive the expression for $f(r_t|r_{t-1};\boldsymbol{\tau})$ in (12). For notational simplicity, we focus on $f(r_2|r_1)$. Starting with $y_{R2}|y_{R1} \sim N(\mu_2 \cos\theta + \alpha(y_{R1} - \mu_1 \cos\theta), \sigma^2)$ and $y_{R1} \sim N(\mu_1 \cos\theta, \sigma^2/(1-\alpha^2))$, and similarly for the imaginary component, and

transforming to magnitude and phase, it can be shown that

(S-16)
$$f(r_1, \phi_1, r_2, \phi_2) \propto \exp[C_1 \cos(\phi_1 - \theta) + C_2 \cos(\phi_2 - \theta) + C_{12} \cos(\phi_1 - \phi_2)],$$

where $C_1 = r_1(\mu_1 - \alpha\mu_2)/\sigma^2$, $C_2 = r_2(\mu_2 - \alpha\mu_1)/\sigma^2$, and $C_{12} = \alpha r_1 r_2/\sigma^2$. First, we integrate with respect to ϕ_2. Writing $C_2 \cos(\phi_2 - \theta) + C_{12} \cos(\phi_1 - \phi_2) = K \cos(\phi_2 - \psi)$, where $K = [C_2^2 + C_{12}^2 + 2C_2 C_{12} \cos(\phi_1 - \theta)]^{1/2}$, and using $\int_0^{2\pi} \exp[K \cos(\phi_2 - \psi)] d\phi_2 = 2\pi \mathbb{I}_0(K)$, we apply the Neumann Addition Formula (Watson, 1948) to write

(S-17)
$$\mathbb{I}_0(K) = \sum_{m=0}^{\infty} \omega_m \mathbb{I}_m(C_2) \mathbb{I}_m(C_{12}) \cos[m(\phi_1 - \theta)],$$

where $\omega_m = 1$ for $m = 0$ and $\omega_m = 2$ for $m \geq 1$. Also, using the result $\int_0^{2\pi} \cos[m(\phi_1 - \theta)] \exp[C_1 \cos(\phi_1 - \theta)] = \mathbb{I}_m(C_1)$, for $m \geq 0$ (Mardia and Jupp, 2000), we obtain $f(r_1, r_2)$. Dividing the result by (S-9), we obtain

(S-18)
$$f(r_2|r_1) = \frac{r_2}{\sigma^2} e^{C_0} \left[\mathbb{I}_0 \left(\frac{r_1 \mu_1}{\gamma_0} \right) \right]^{-1} \sum_{m=0}^{\infty} \omega_m \mathbb{I}_m(C_1) \mathbb{I}_m(C_2) \mathbb{I}_m(C_{12}),$$

where $C_0 = -[r_2^2 + \mu_2^2 + \alpha^2(r_1^2 + \mu_1^2) - 2\alpha\mu_1\mu_2]/(2\sigma^2)$.

S-2.4.3. *Supplement to Section 3.3 – Calculating the AR(1) log-likelihood function at high SNRs is computationally prohibitive.* The following simulation study demonstrates that calculation of the Ricean AR(1) log-likelihood function (12) becomes increasingly computationally prohibitive as the SNR increases. To vary the SNR over the range of values seen in the dataset over different amounts of spatial smoothing, we generated magnitude time series from the Ricean AR(1) model with the $\boldsymbol{X}$ matrix described in Section 2.2, and β_0 varied over $\{2^j : j \in \mathbb{Z}, 0 \leq j \leq 7\}$. Other parameter values of $\sigma^2 = 1$, $\alpha = 0.3$, and $\beta_1 = 0$ were held constant.

After the parameter estimates for each simulated time series were calculated using the hybrid EM/NR algorithm, we timed the calculation of the Wald and LRT statistics. Timing results are from a Intel Core i5-6300M CPU 64-bit processor running `C` within `R` (R Core Team, 2020). Figure S-7(a) shows that the calculation time of the LRT statistic is uniformly higher than the Wald test statistic and increases with the SNR. The computational time starts to become prohibitive from SNRs at around 30, when it is aproximately 1 second per time series, and increases further from there. As suggested by Figure S-7(b), this increase in computation time is due to the increase in terms of the sum $\sum_{m=0}^{\infty} \omega_m \mathbb{I}_m(C_1) \mathbb{I}_m(C_2) \mathbb{I}_m(C_{12})$ in (12) necessary for convergence (defined as a change of less than 10^{-10}). As a result, we will restrict our use of the LRT statistic to SNRs below 10 and use the Wald test statistic otherwise (where the false positive rate problem illustrated in Figure S-6 does not appear to be an issue).

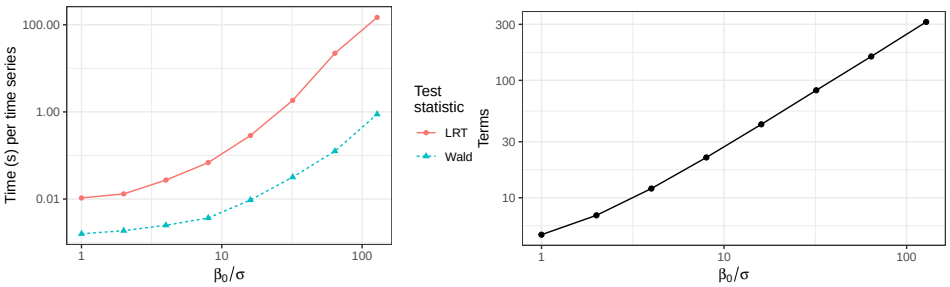

(a) Calculation time (b) Number of terms

FIG S-7. *(a) The calculation time for the LRT statistic is greater than the Wald test statistic, becoming prohibitive for high SNRs. (b) The average number of terms of the sum* $\sum_{m=0}^{\infty} \omega_m I_m(C_1) I_m(C_2) I_m(C_{12})$ *needed for convergence increases with SNR as well. (Note: Both plots use log scales.)*

S-2.5. *Supplement to Section 3.4 – Choosing the order of the AR model.* We performed a simulation study to compare the AR orders detected under the sequential testing method proposed in Section 3.4 with those detected under the AIC and BIC (Akaike, 1973; Schwarz, 1978) – *i.e.,* more common model selection criteria. We generated 10,000 time series under the CV model with $\boldsymbol{X}$ matrix described in Section 2.2, $\boldsymbol{\beta} = (5, 0)'$, $\sigma^2 = 1$, and four sets of different AR coefficients: (1) $\alpha = 0$ for temporal independence, (2) $\alpha = 0.1$ and (3) $\alpha = 0.2$ for AR(1) dependence, and (4) $\boldsymbol{\alpha} = (0.1, 0.1)'$ for AR(2) dependence. The proportions of time series detecting each AR order $\widehat{p}$ based on the AIC, BIC, and sequential testing method using a significance level of $\delta = 0.01$ under the three models are shown in Figure S-8.[2]

Two main results are worthy of special attention: first, the sequential testing method in general detects a similar distribution of orders as the AIC and BIC. The BIC is more similar to the sequential method, which can be explained by the fact that the BIC penalty for each additional parameter of $\log n = 6.43$ in this case is closer to the sequential testing threshold of $\chi^2_{1,0.99} = 6.63$ than the AIC penalty of 2. The second result is that the MO data-based order detection methods are more likely to have a negative bias, and under-detect orders (in this case, especially for $\alpha = 0.1$ and $\boldsymbol{\alpha} = (0.1, 0.1)'$) than the CV model-based method. This difference can be attributed to the fact that CV model has twice the amount of data, which gives it more power in the sequential testing method.

S-3. Supplement to Section 4 – Further Simulation-based analyses.

S-3.1. *Supplement to Section 4.1 – Properties of parameter estimates.* Figure S-9 expands on the results in Figure 2, summarizing the biases, standard errors, and

[2]Note that MOR model results are not shown for the AIC and BIC because the MOR model log-likelihood is not tractable for general p.

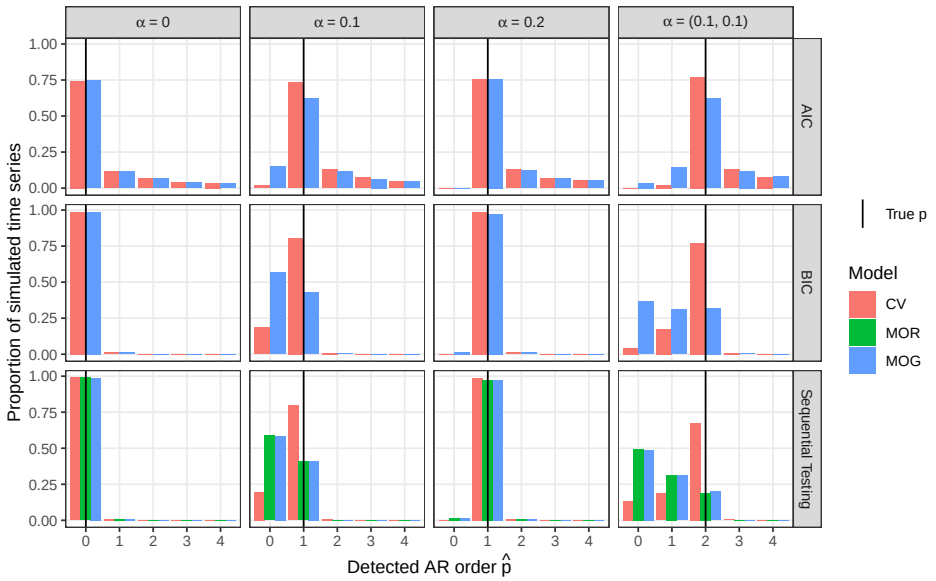

FIG S-8. *Proportion of simulated time series in which each AR order (0-4) is detected for four different sets of AR coefficients (columns), based on the AIC, BIC, and sequential testing methods (rows) and the three models (colored bars). Note that MOR model results are not shown for the AIC and BIC because the MOR model log-likelihood is not tractable for general p.*

root mean squared errors of $\widehat{\beta}_0$, $\widehat{\beta}_1$, $\widehat{\sigma}^2$, and $\widehat{\alpha}$ under the three models for simulated values of $\alpha = 0.2$, 0.4, 0.6, and 0.8. (Figure 2 only shows $\alpha = 0.4$.) Qualitative comparisons of the parameter estimate properties across models (which models are better/worse) are consistent across different values of α.

S-3.1.1. *Supplement to Section 4.2 – Missing information matrix.* The Fisher information matrix is commonly used to estimate the standard errors of parameter estimates (Casella and Berger, 2002) and in-so-doing, quantify the amount of "information" given in the data about a parameter. In the framework of the EM algorithm, separate information matrices can be derived based on the complete, observed, and missing data (McLachlan and Krishnan, 2008). This extension allows us to quantify the amount of "missing information" in the missing data about a parameter (Orchard and Woodbury, 1972). In our context, recall that the magnitude, phase, and magnitude-phase constitute the observed, missing, and complete data, respectively. Thus, by deriving the missing information matrix, we can quantify the amount of "missing information" in the phase we miss out on when using magnitude-only data.

For simplicity, consider a single complex-valued measurement, with magnitude r and phase ϕ. We assume that the real and imaginary components y_R and y_I are independent and normally distributed, with means $\mu \cos\theta$ and $\mu \sin\theta$, respectively,

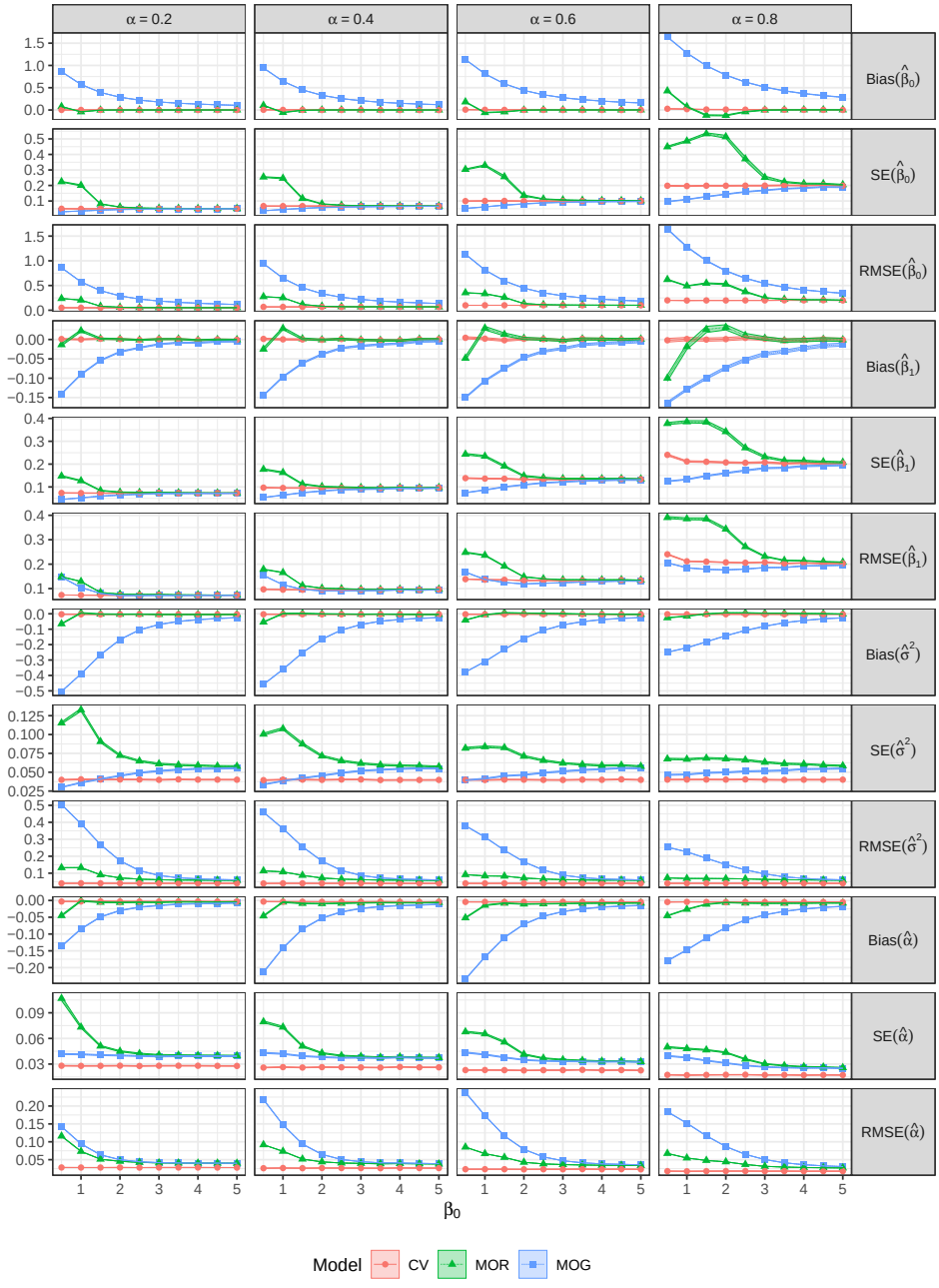

FIG S-9. *Biases, SEs (SE), and RMSEs (RMSE) of* $\widehat{\beta}_0$, $\widehat{\beta}_1$, $\widehat{\sigma}^2$, *and* $\widehat{\alpha}$ *under three models for simulated time series under* $\beta_1 = 0.2$, *and different values of* β_0 *and* α. *The shaded areas cover the estimate* $\pm$ *2 standard error intervals.*

and identical variances σ^2. The log-likelihood function of the observed data r is equal to that of the complete data (r, ϕ) minus the missing data ϕ; that is,

$$\log L(\boldsymbol{\tau}; r) = \log L_c(\boldsymbol{\tau}; r, \phi) - \log k(\phi|r; \boldsymbol{\tau}). \tag{S-19}$$

Differentiating with respect to $\boldsymbol{\tau}$ twice and obtaining its expectation with respect to ϕ, conditional on r, gives the following relationship between the information matrices:

$$\mathscr{I}(\boldsymbol{\tau}; r) = \mathscr{I}_c(\boldsymbol{\tau}; r) - \mathscr{I}_m(\boldsymbol{\tau}; r). \tag{S-20}$$

In words, the observed information is equal to the complete information minus the missing information.

It can be shown that observed-, complete-, and missing-data log-likelihoods are

$$\log L(\boldsymbol{\tau}; r) = -\log \sigma^2 - \frac{r^2 + \mu^2}{2\sigma^2} + \log \mathbb{I}_0\left(\frac{\mu r}{\sigma^2}\right) \tag{S-21}$$

$$\log L_c(\boldsymbol{\tau}; r, \phi) = -\log \sigma^2 - \frac{r^2 + \mu^2}{2\sigma^2} + \frac{\mu r}{\sigma^2}\cos(\phi - \theta) \tag{S-22}$$

$$\log k(\phi|r; \boldsymbol{\tau}) = -\log I_0\left(\frac{\mu r}{\sigma^2}\right) + \frac{\mu r}{\sigma^2}\cos(\phi - \theta), \tag{S-23}$$

respectively. For simplicity, suppose it is known that $\sigma^2 = 1$. Then, differentiating twice with respect to μ shows that the complete- and missing-data information matrices are $\mathscr{I}_c(\mu; r) = 1$ and $\mathscr{I}_m(\mu; r) = \frac{\partial^2}{\partial \mu^2} \log \mathbb{I}_0(\mu r)$, respectively. It can be shown that

$$\mathscr{I}_m(\mu; r) = r^2 - r\mathbb{A}(\mu r)/\mu - r^2\mathbb{A}^2(\mu r), \tag{S-24}$$

where $\mathbb{A}(\cdot) = \mathbb{I}_1(\cdot)/\mathbb{I}_0(\cdot)$ as before.

After averaging over the Rice(μ, 1) distribution of R using Monte-Carlo integration, these information matrices are displayed in Figure 5. Note that the fraction of the complete-data (total) information provided by the magnitude-only data increases as the SNR increases.

Interestingly, the rate of convergence of the EM algorithm is a function of the missing- and complete-data information matrices (Dempster, Laird and Rubin, 1977). Specifically, defining the rate of convergence as $r_c = \lim_{k\to\infty} ||\boldsymbol{\tau}^{(k+1)} - \widehat{\boldsymbol{\tau}}||/||\boldsymbol{\tau}^{(k)} - \widehat{\boldsymbol{\tau}}||$, it can be shown that r_c is given by the largest eigenvalue of $\boldsymbol{\mathcal{I}}_c^{-1}(\widehat{\boldsymbol{\tau}}; \boldsymbol{r}, \boldsymbol{\phi})\boldsymbol{\mathcal{I}}_m(\widehat{\boldsymbol{\tau}}; \boldsymbol{r})$. This information ratio matrix measures the proportion of information about $\boldsymbol{\tau}$ that is missing by not also observing $\boldsymbol{\phi}$ in addition to $\boldsymbol{r}$ (McLachlan and Krishnan, 2008, Section 3.9.3). The greater the proportion of missing information, the slower the rate of convergence. We then see a connection between the large proportion of missing information at low SNRs in Figure 5 and the higher computation times of the MOR model at low SNRs in Figure S-5. As the SNR increases, the proportion of missing information decreases and so does the computation time.

S-4. Supplement to Section 5 – Further Analysis of low-SNR Dataset.

S-4.1. *Supplementary figures.* The following figures are presented in the order to which they are referred in the main article. Figure S-10 shows the frequency distributions of the voxel-wise detected AR orders under the three models. The

FIG S-10. *Frequency distributions of detected AR orders for the fingertapping dataset under the three models.*

orders were detected using the sequential testing procedure described in Section 3.4 with a significance level of 0.01. The orders were limited to a maximum of 4 due to large computational times using the MOR model; if a larger cap on orders is desired in practice, we suggest using the MOG model as a surrogate, as it gives very similar results without such computational issues.

Figure S-11 expands on the results of Figure 6, showing activation maps for slices 1, 2, and 3 with inset maps showing the left central sulcus ROI. (Figure 6 only shows slice 2.) These additional slices are shown to demonstrate that the maps shown of slice 2 in Figure 6 show more activation than the other slices, but the patterns of activation are somewhat similar across all slices. In addition, Figure S-12 provides a graphical representation of the p-values in Table 2.

Figure S-13 refers to our study of adding extra noise to the original unsmoothed data to further lower the SNR and CNR of the dataset. The plots show the average SNRs and CNRs for 10,000 simulation-based time series generated from each of the 10 voxel time series identified in Figure 6. The results verify that adding extra noise to the raw data does indeed lower the SNRs and CNRs and that the effect is intensified as the noise standard deviation σ_a increases. Also, Figure S-14 shows a graphical representation of the detection proportions in Table 3.

References.

ABRAMOWITZ, M. and STEGUN, I. (1965). *Handbook of Mathematical Functions*. Dover Publications.

ADRIAN, D. W., MAITRA, R. and ROWE, D. B. (2018). Complex-valued time series modeling for improved activation detection in fMRI studies. *Annals of Applied Statistics* **12** 1451-1478.

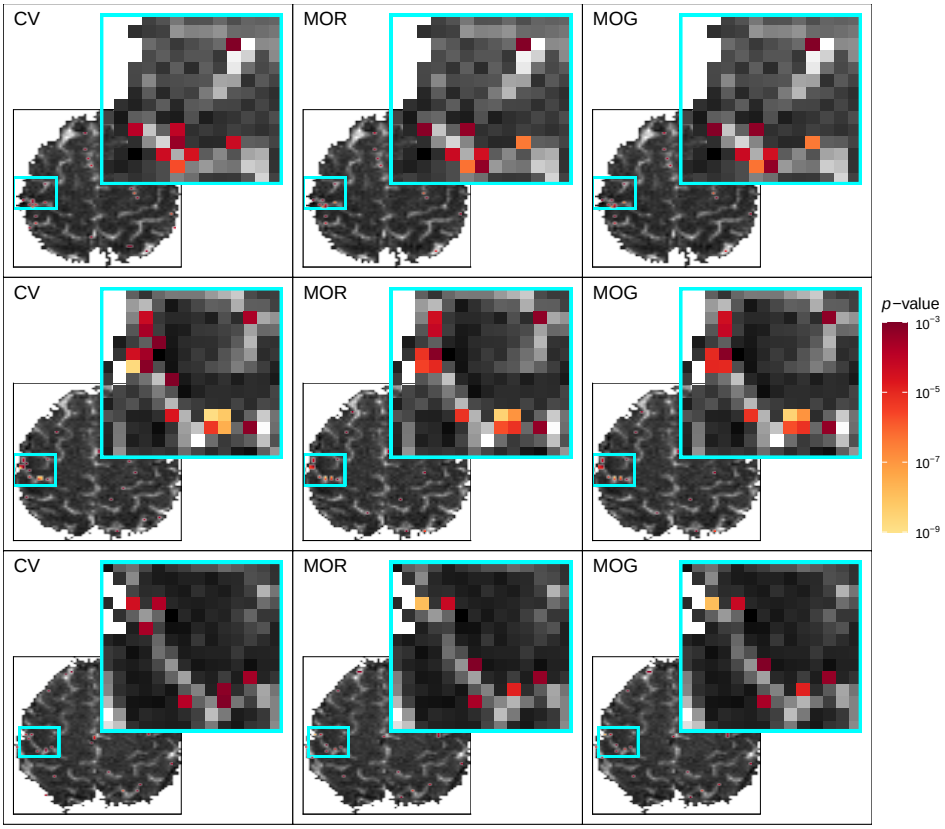

FIG S-11. *Activation maps for (by row, from top) slices 1, 2, and 3.*

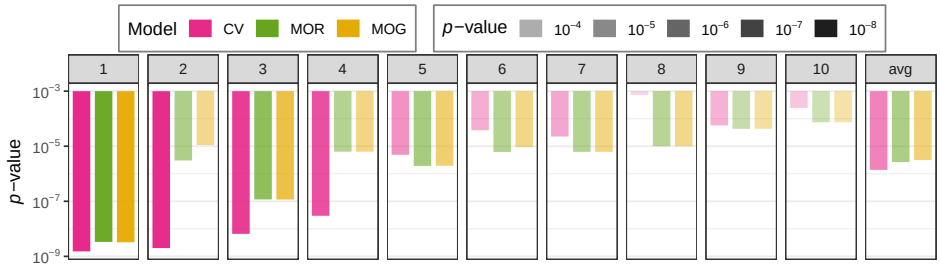

FIG S-12. *Graphical representation of the p-values in Table 2. (The shading represents the strength of the p-values.)*

AKAIKE, H. (1973). *2nd International Symposium on Information Theory* Information theory and an extension of the maximum likelihood principle 267-281. Akademiai Kiado.

CASELLA, G. and BERGER, R. L. (2002). *Statistical Inference*, Second edition ed. Thomson Learning.

COCHRANE, D. and ORCUTT, G. (1949). Applications of least squares regression to relationships containing autocorrelated errors. *Journal of the American Statistical Association* **44** 32-61.

DEMPSTER, A. P., LAIRD, N. M. and RUBIN, D. (1977). Maximum likelihood from incomplete

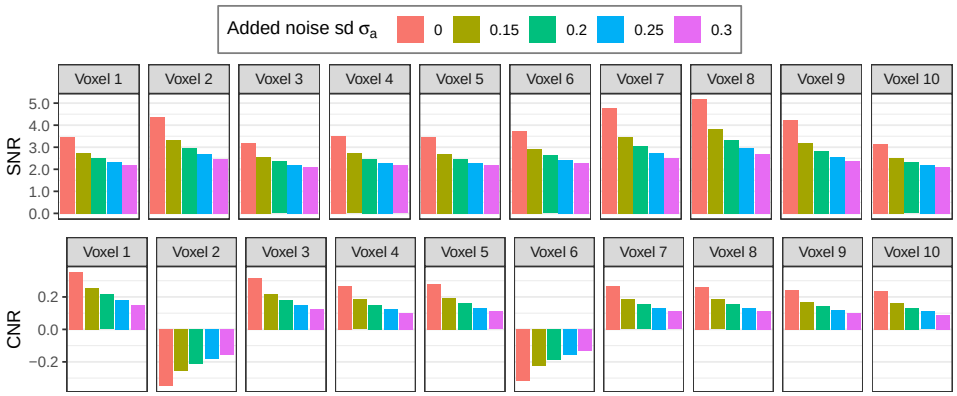

FIG S-13. *The SNRs and CNRs of the ten voxels identified in Figure 6 decrease when extra noise with standard deviation σ_a is added to the raw data ($\sigma_a = 0$ refers to raw data).*

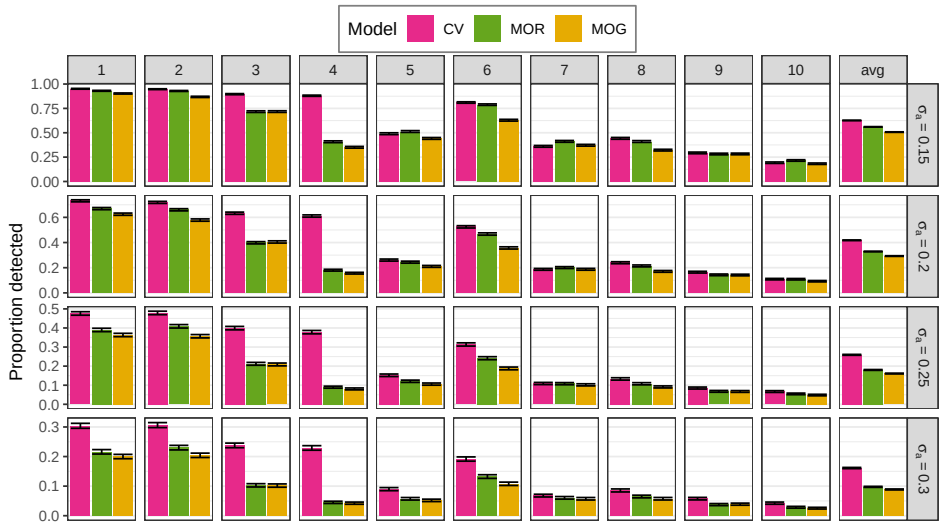

FIG S-14. *Proportion of replications the 10 voxels (and average proportion "avg") identified in Figure 6 (columns) detected as activated when noise with standard deviation σ_a (rows) was added to the raw data. The error bars show estimate $\pm$ 2 standard errors.*

data via the EM algorithm. *Journal of Royal Statistical Society Series B* **23** 1-38.

GENOVESE, C. R. (2000). A Bayesian Time-Course Model for Functional Magnetic Resonance Imaging Data. *Journal of the American Statistical Association* **95** 691–703. Available at http://www.jstor.org/stable/2669445

GLOVER, G. H. (1999). Deconvolution of impulse response in event-related BOLD fMRI. *NeuroImage* **9** 416-429.

HASTIE, T., TIBSHIRANI, R. and FRIEDMAN, J. (2009). *The elements of statistical learning: data mining, inference and prediction*, 2 ed. Springer. Available at http://www-stat.stanford.edu/~tibs/ElemStatLearn/

MARDIA, K. V. and JUPP, P. E. (2000). *Directional Statistics*. Wiley.

MCLACHLAN, G. J. and KRISHNAN, T. (2008). *The EM Algorithm and Extensions*. Wiley.
MILLER, J. W. (1995). Exact Maximum Likelihood Estimation in Autoregressive Processes. *Journal of Time Series Analysis* **16** 607-615.
ORCHARD, T. and WOODBURY, M. A. (1972). A missing information principle: theory and applications. In *Proceedings of the Sixth Berkeley Symposium on Mathematical Statistics and Probability* **1** 697-715. University of California Press, Berkeley, California.
POURAHMADI, M. (2001). *Foundations of Time Series Analysis and Prediction Theory*. Wiley.
R CORE TEAM, (2020). R: A Language and Environment for Statistical Computing, Vienna, Austria.
RICE, S. O. (1944). Mathematical analysis of random noise. *Bell Systems Technical Journal* **23** 282.
SCHWARZ, G. E. (1978). Estimating the dimension of a model. *Annals of Statistics* **6** 461-464.
TANABE, J., MILLER, D., TREGELLAS, J., FREEDMAN, R. and MEYER, F. G. (2002). Comparison of Detrending Methods for Optimal fMRI Preprocessing. *Neuroimage* **15** 902–907. Available at https://doi.org/10.1006/nimg.2002.1053
WATSON, G. N. (1948). *A Treatise on the Theory of Bessel Functions*. Cambridge University Press.

DEPARTMENT OF STATISTICS
GRAND VALLEY STATE UNIVERSITY
ALLENDALE, MI 49401-9403
USA
E-MAIL: adriand1@gvsu.edu

DEPARTMENT OF STATISTICS
IOWA STATE UNIVERSITY
AMES, IA 50011-1090
USA
E-MAIL: maitra@iastate.edu

DEPARTMENT OF MATHEMATICAL AND STATISTICAL SCIENCES
MARQUETTE UNIVERSITY
MILWAUKEE, WI 53233
USA
E-MAIL: daniel.rowe@marquette.edu